University of Alberta

Synthesis, Characterization and Biological Studies of the Phospholipid Coated Gold Nanoparticles (GNPs)

by

Meijing Wang

A thesis submitted to the Faculty of Graduate Studies and Research
in partial fulfillment of the requirements for the degree of

Master of Science

Department of Chemistry

Fall 2013
Edmonton, Alberta

ABSTRACT

Gold nanoparticles (GNPs) have been applied as diagnostic and therapeutic agents because they can be targeted, localized, and be heated to cause cell death. However, their use has been limited by their relatively low biocompatibility. In this work, we coated the GNPs surface by a biocompatible phospholipid bilayer composed of 1-stearoyl-2-oleoyl-*sn*-glycero-3-phospho-(1'-*rac*-glycerol) (SOPG). In order to use the fluorescence, a small amount of the NBD labeled PG (NBD-PG) was introduced to the phospholipid bilayer. We synthesized and characterized the NBD labeled SOPG coated GNPs (NBD-SOPG-GNPs) and gold nanorods with different size and shape. We tested the interaction of 30 nm NBD-SOPG-GNPs with three different cell lines (A549, C2C12 and C2bbe1) to investigate their uptake and intracellular fate as well as the response of the cells to the presence of the NBD-SOPG-GNPs. Our results demonstrated that NBD-SOPG-GNPs has different uptake destinations in three cell lines.

ACKNOWLEDGEMENTS

First of all, I would like to express my special gratitude and thanks to my supervisor, Dr. Nils O. Petersen, who has provided me with valuable guidance and support through my learning process of this Master thesis.

I would also like to specifically thank Uyen Ho, Liang Shuai, Guihua Zhou, Lei Pei, Belete Legesse, Hao Yu, Huiying Sheng, Mahanmud Ahamud, Ya Zhou, Kumakshi Sharma, Jaeyong Cho, Weizheng (Wendy) Shen, Rahul Agrawal, Lindsay Shearer, Max Anikovskiy, Yaxin Jiang, Chunhong Tian, Xi Li, Julian Diaz, Jiahui Wu, Yi Shen, Yidan Ding, Nada Djokic, Feng Jia, Urmi Bhusan Bhakta, Yiman Wu, Bethany Griffith, Daniel Salamon, de Guzman Catherine, Brigley Angela, Parnian Lak, Jing Li, Juan Bravoj, Spencer Alford, Feng Li, Zonglin Yang for kindly support and helpful advice during my time in the graduate school.

I would like to thank Dr. Julie Qian, Dr. Jian Chen, Dr. Mike Xia, Ms. Pinzhang (Priscilla) Gao, Ms. Jingyi Yang, Dr. Xuejun Sun, Ms. Gerry, Ms. Nancy Zhang for the helpful technical assistance during my research. And I want to thank Dr. Christopher Cairo, Dr. Robert Campbell, Dr. Mark McDermott and Dr. Michael Woodside for their valuable advices and kindly help.

Finally, I would like to thank my family, especially my parents and my lovely niece, for their understanding and support.

Table of Contents

LIST OF TABLES

LIST OF FIGURES

LIST OF ABBREVIATIONS

AA Ascorbic acid

Anti-pmp70 Anti peroxisomal membrane protein 70

BF Bright field

CCVs Clathrin coated vesicles

CD Cluster density

CDr Cluster density of red particles

CDg Cluster density of green particles

CTAB Cetrimonium bromide

DLS Dynamic light scattering

DiI-SOPG-GNPs DiI labeled SOPG coated gold nanoparticles

DiI (2Z)-2-[(E)-3-(3,3-dimethyl-1-octadecylindol-1-ium-2-yl)prop-2-enylidene]-3,3-dimethyl-1-octadecylindole, perchlorate

DM Desktop microscopist

EM Electron microscopy

GNPs Gold nanoparticles

ICCS Image cross correlation spectroscopy

ICS Image correlation spectroscopy

LBs Lamellar bodies

mAb Monoclonal Antibody

MVBs Multivesicular bodies

NBD-SOPG-GNPs NBD labeled SOPG coated gold nanoparticles

NBD-PG 1-oleoyl-2-{12-[(7-nitro-2-1,3-benzoxadiazol-4-yl)amino] dodecanoyl}-*sn*-glycero-3-[phospho-*rac*-(1-glycerol)]

NBD 7-nitro-2-1,3-benzoxadiazol-4-yl

NINT National Institute for Nanotechnology

NPs Nanoparticles

PBS Phosphate buffered saline

PEG Polyethylene glycol

PF Paraformaldehyde

PPT Photothermal therapy

ROS Reactive oxygen species

RT Room temperature

RFP Red fluorescent protein

SE Secondary electrons

SEI Secondary electron imaging

SPR Surface plasmon resonance

SEM Scanning electron microscope

SEM Standard error of the mean

SOPG 1-stearoyl-2-oleoyl-*sn*-glycero-3-phospho-(1'-*rac*-glycerol)

TEM Transmission electron microscope

TPPMS Triphenylphosphine monosulfonate

UV-Vis spectroscopy UV-Visible spectroscopy

Chapter 1 Gold nanoparticles: properties and applications

1.1 Introduction of nanoparticles (NPs)

Nanoparticles have gained great scientific interests because they possess various advantages compared to the bulk materials, which make them more ideal for the biological applications. Bulk metal materials usually possess constant physical properties; however, size dependent physical properties of NPs are often monitored. For example, the physical and chemical properties of nanomaterials can be significantly changed by a target binding event, which may not happen to a bulk structure that is composed of the same material. [1] Furthermore, the size of NPs is 1-100 nm, which is at the comparable size to the proteins in cells. [2] This property enables the NPs to interact with cellular compartments and molecules more efficiently. Moreover, NPs are very small in size which enables them to confine electrons and generate quantum effects. These resulting physical and chemical properties of NPs are different from the bulk structures and molecular compounds composed of the same material. [3] For example, 1-10 nm GNPs solution shows dark ruby color. And this optical property strongly depends on the size, shape, composition and nature of the capping compounds. For example, when a light hit on the surface of nanomaterials, different phenomenon will show up which makes these materials ideal for some analyte detections. [4] At last, the large surface to volume ratio of NPs provides high density loading of the drugs, which is very useful in the targeting delivery.

NPs have been applied in the biological sciences, such as the conjugation with DNA, peptides and proteins, for very long time. [5, 6] We have seen great growth of nanomaterials engineering, such as nanotubes, nanowires and nanofibers in the

past few years. [7-9] Furthermore, we have observed impressive advances in the techniques and methods of engineering materials, such as size control, patterning and surface modification. [10, 11]

1.2 Gold nanoparticles (GNPs) and its biomedical applications

GNPs are chemically inert in cells and have been widely used in humans for the last 60 years. GNPs were firstly introduced by Michal Faraday, who expressed the multicolour gold solution by the synthesis of gold chloride and sodium citrate. [12] And after that, GNPs started to be used in science and medicine. In the late 1950s, researchers found that proteins bound to GNPs didn't change their functions, which lead to the application of GNPs in immunodiagnostics and histopathology. [13] Nowadays, GNPs have been used in diagnostics by assembling to a scaffold to support the DNA. [6] GNPs are also used in the treatment of cancer radiotherapy and tumor target nano therapy. [14, 15] Many studies have proved the promising potential of the GNPs in the bioimaing, biosensing, targeting delivery and cancer therapy. (Figure 1.1) [16]

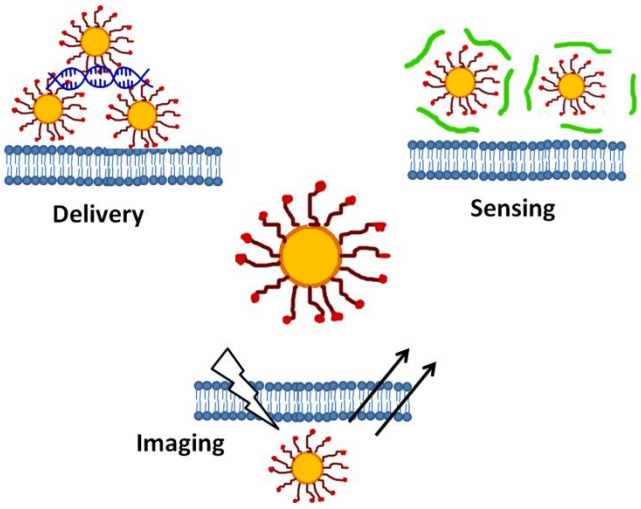

Figure 1.1. Different potential applications of GNPs in biomedical research. [Adapted from reference 16]

GNPs in the applications of biosensors and bioimaging

The free electrons in the conduction band provide the GNPs with a series of unique and important optical properties. When light hits the GNPs, the surface properties of GNPs become dominant. The electric field of the light can induce coherent oscillation of the free electrons in conduction band. This property is often referred as surface plasmon resonance (SPR), which depends on the size, shape and materials of the GNPs. Thus, any change such as surface modification and aggregation will cause the colorimetric changes of the GNPs solution. [17] The most obvious example is the noticeable color change upon the aggregation of GNPs, which is due to the coupling of the plasmons. This effect has been widely explored and has important application in the colorimetric sensors. [18]

There are extensive reports about the detection of DNA using GNPs. [19] Hill et al. introduced a new form of the bio-barcode assay for the detection of double stranded DNA by inhibiting the target rehybridization by blocking strands. [20]

Dai et al. developed a one-step method to detect DNA by using GNPs combined with dynamic light scattering. [21] This method has high sensitivity and is easy to conduct because it excludes the separation and amplification step. Furthermore, when a light hit on the particles, the light is not only absorbed by the plasmon, but also scattered by the particles. Thus it is possible to track the movement of the individual GNP when the scattered light is in the visible range. [22]

GNPs can scatter many colors when it is illuminated by a white light. This effect enables GNPs to be used as a contrast agent in the biomedical imaging. As a contrast agent, GNPs possess several unique properties compared with other contrast agents in cellular imaging. Firstly, GNPs have higher extinction coefficient, which makes them scatter intensely and brighter to give high contrast. Furthermore, GNPs are chemically inert in cells, which makes them more suitable for the biomedical applications. The size and shape of GNPs are controllable and they can be detected at very low concentration, such as 10^{-16} M.

GNPs in potential cancer therapy

GNPs are much smaller in size comparing to the cells and they are even smaller than the enzymes, antibodies and receptors in cells. This allows the GNPs to interact with these biological molecules efficiently on the surface and inside of the cells, which could be very useful in the cancer diagnosis and therapy. The most conventional treatments of cancer are surgery, photothermal therapy (PPT) and chemotherapy. Nowadays, GNPs have been widely used to destruct cancer and tumor cells in the PPT. The irradiation of GNPs at ‘water window’ (800-1200 nm) can result in minimum damage to the biological tissue. Thus, targeted GNPs can

be used to destroy only cancer cells when illuminated by a laser at a suitable wavelength range. [23]

After irradiation, the excited conduction band electrons jump back to the ground state and release energy, which will heat the surrounding medium and kill cells in neighbourhood. [24] The temperature of this method can reach up to 1000 °C, depending on the concentration of GNPs, irradiation time and laser power. [25] The photothermal effect is the fundamental basis of the application of GNPs in cancer phototherapy. Huang et al. have showed that the photothermal activity was enhanced by 20 times when use the GNPs. [23]

GNPs in the application of drug delivery

GNPs can also serve as a good scaffold in the drug delivery because they are nontoxic and stable in cells. Furthermore, GNPs can be easily synthesized and functionalized by amine or thiol group which enable the surface modifications with DNA, peptides and amino acids for the biological applications. The controlled synthesis of GNPs with various sizes has been well established. [16] The multifunctional monolayer of GNPs can be well fabricated using ligand-exchange reactions. [26] This tenability property provides GNPs surface to have multiple chemotherapeuitcs and/or targeting agents. This structure diversity also enables GNPs with the potential in the targeting and stability/release drug delivery system. For example, hydrophobic drugs can be combined to GNPs by hydrophobic interaction, which has no requirement of structure modification in the drug loading or drug release. Covalent bond can provide strong binding between the drugs and GNPs and is usually used when a stable linkage is required.

The covalent conjugation through cleavage linkages can be release to cells by external or internal stimuli. (Figure 1.2) [27]

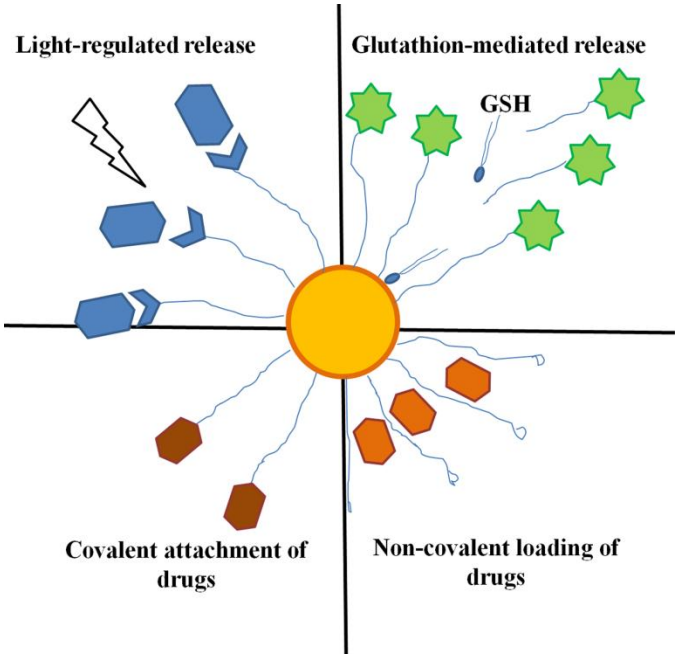

Figure 1.2. GNPs can provide effective bindings to different drugs and control the drug release by different reactions. [Adapted from reference 27]

1.3 Disadvantages of GNPs in biomedical application

Many bulk materials are non-toxic, but become toxic when their size is decreased to nanoscale. The toxicity of the GNPs has been studied extensively at the cellular level and GNPs have been showed to enter cells in a manner highly related to their size, physical dimensions and surface modifications. [28] GNPs can be taken up by cells efficiently and most results shows they have low toxicity to cells. [29, 30] However, more results show the surface coating of GNPs plays an important role to cause the cytotoxicity of GNPs. [31] For example, Conner et al. investigated the cytotoxicity of the GNPs with different surface modifications in human leukemia (K562) cells. [32] These surface modifiers include biotin,

cysteine, citrate, CTAB and glucose. Their results showed that the glucose and cysteine coating caused higher cytotoxicity while the citrate and biotin tended to maintain a low toxicity after 3 days exposure. Wan-Seob Cho et al. studied the *in vivo* toxicity of 13 nm sized GNPs coated with PEG (MW 5000). They found the 13 nm PEG-coated GNPs caused transient inflammatory response and induced the apoptosis after the injection. [33]

Cytotoxicity may not be the only harmful effect of GNPs, other non-cytotoxic effects, such as the decrease in proliferation and change in morphological structure, should also be considered. Nadine Pernodet et al. investigated the adverse effects of 14 nm citrated coated GNPs on the human dermal fibroblasts. They found that the citrated coated GNPs caused the anomalous actin filaments and extracellular matrix, which in turn reduced the cell proliferation, mobility and adhesion. [34] The number of vacuoles also increased after the treatment and cells were packed with vacuoles after six days. [34]

Oxidative stress is one of the most noticeable features of GNPs toxicity. A small amount of the oxidative stress will be neutralized by the cellular antioxidant defence system. Mild excess of oxidative stress can trigger the inflammatory pathways, while excessive production of oxidative stress will lead to cell death by oxidizing cellular components, such as cell membrane lipids, proteins and DNA. [35] Yu Pan et al. showed surface chemistry of GNPs was an essential way to determine to the cytotoxicity of GNPs. They found that the 1.4 nm triphenylphosphine monosulfonate (TPPMS) coated GNPs caused cell death by increasing the oxidative stress, which was enlarged by the mitochondrial damage.

The genome-wide expression profiling also indicated the robust upregulation of the stress related genes after a few hours incubation. [36] Libo Du et al. found 13 nm citrate coated GNPs caused nitric oxide stress, which can lead to cell death by triggering the oxidative and nitrosative stress. [37]

The control of cell cycle is also essential for the growth and normal function of cells. The cell cycle is consisted of four distinct phases, G1 phase, S phase, G2 phase and mitosis. G0/G1 and G2/M are two important checkpoints, which ensure no damage DNA is passed to cells of next generation. The stage of the cell cycle can be determined by quantifying the DNA amount. The cell proliferation will be reflected by the DNA amount and the ratio change of G1 and G2 phase. Wilson Roa et al. showed the glucose capped GNPs caused the prostate cancer cells cycle to accelerate in the G0/G1 phase and accumulate in the G2/M phase. [38]

Furthermore, GNPs also serve as an ideal model to solve the problem of size dependent toxicity. In 2006, Born and Muller-Schulte recognized the increasing toxicity of nanoparticles caused by its physical dimensions. [39] S. Vijayakumar and S. Ganesan showed the cell viability of nanoparticles treated cells were related to the size of citrate coated GNPs. The results showed that the citrate stabilized GNPs with size of 3 nm, 8 nm and 30 nm caused gradual cell death within 24 hrs at higher concentration. [40] Christian Freese et al. studied the effect of citrate coated GNPs with different size (10 nm, 11 nm and 25 nm) on the viability of endothelial and epithelial cells. They found that the higher amount of citrate on the particle surface (25 nm citrate coated GNPs) cause the higher

reduction of the cell viability, but didn't impair the uptake behavior of the cells. [41]

Cetyl trimethylammonium bromide (CTAB) is another common capping reagent for the GNPs or gold nanorod, in which CTAB form a bilayer on the surface of the GNPs and can direct gold nanorod to grow in one direction. [42] The CTAB give the gold nanorod a high positive charge. Marco Tarantola et al. discovered the CTAB coated GNPs (42.9 ± 4.0 nm) were high toxic to MDCK II cell and generated adverse effects, such as the generation of reactive oxygen species (ROS) and impairment of the cytoskeleton integrity. They also found the CTAB coated gold nanorod with a length of 37.8 ± 6.5 nm and a width of 17.2 ± 2.9 nm also caused cytotoxicity to cells, but generally less toxic than the spherical GNPs. [43] CTAB alone is very toxic to cell, free CTAB molecules in GNPs solutions can come from the inadequate purification or desorption of the surfactant on the surface of the GNPs. Thus, some researchers argued that the apparent toxicity of CTAB coated gold nanorod was from the free CTAB in the solution, but not the gold nanorod themselves. [44] In this paper, Marco Tarantola et al. proposed that the higher toxicity of the CTAB coated spherical GNPs was due to the aggregation or cluster formation, and subsequently lead to the realease of the CTAB to the cell interior and cause a secondary toxicity.

Thus, in conclusion, the surface coating of GNPs plays an important role in the cytotoxicity of GNPs in the cells. And the biomedical applications of GNPs are highly restricted either by the low biocompatible surface or the free toxic molecules left in the solution. But in theory, the low biocompatibility of GNPs

can be improved by the surface modification with some more biocompatible materials.

1.4 Liposomes for drug delivery

Liposomes are artificially vesicles which can retain water soluble drugs in the inner core and hydrophobic drugs in the bilayer walls. [45] Liposomes are made of phospholipid bilayer, which is similar to the bilayer construction of cell membrane. This is because of the unique composition of the phospholipid, which contains a hydrophilic head and a hydrophobic tail. When the phospholipid dissolves in the water, the hydrophobic tail will quickly distance from the water. So, the phospholipids will form a double layered membrane as all of the hydrophobic tail stay away from water and all of the hydrophilic head point towards water. (Figure 1.3) Liposomes are usually made by votexing the phospholipids with cargoes to allow vesicles to grow around cargoes.

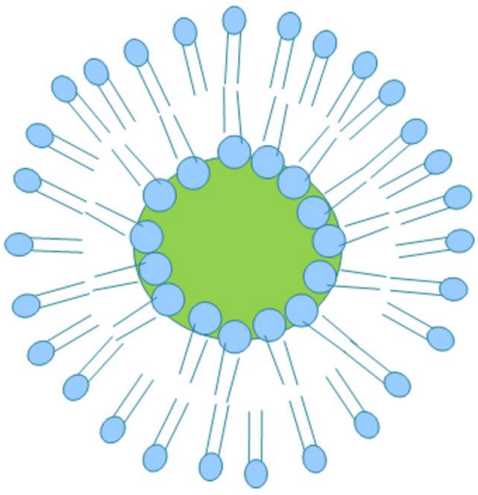

Figure 1.3. Unilamellar liposome formed by phospholipid.

Liposomes can be categorized based on their lamellarity to unilamellar vesicles, oligolamellar vesicles and multilamellar vesicles. Unilamellar vesicles contain

one lipid bilayer and generally have a size between 50-250 nm. They are preferentially applied to encapsulate water soluble drugs because of their large aqueous core. Multilamellar vesicles contain several lipid bilayers and have a diameter of 1-5 μm. The multilamellar vesicles can passively trap the hydrophobic drugs because of their high concentric lipid components. Liposomes also can be classified according to the size (small, intermediate or large vesicles) or based on the preparation methods. [47]

Liposomes have very high biocompatibility and some of them have reached the market or are under the clinical trials. For example, Ambisome® (Gilead Sciences, Foster City, CA, USA) is a lipid based formulation that capsulates the antifungal amphotericin B. [48] Daunoxome® (Gilead Sciences) is a Daunorubicin citrate liposome which comprises daunorubicin in smaller liposomes composed of different lipid compositions. [49] Myocet® (Elan Pharmaceuticals Inc., Princeton, NJ, USA) is a non-pegylated liposomal system which contains anticancer agent doxorubicin. [50]

Liposomes are nontoxic, biodegradable and biocompatible. Liposomes encapsulate drugs either in the aqueous core or the layers and provide a protection to drugs from the external environment. This protection also works as a sustainable release mechanism for drugs and protects sensitive areas from drugs to avoid undesirable side effects. The surface properties of liposomes, such as size and charge, can be easily modified by changing the ingredients of the lipid mixture. [51] Furthermore, the head and tail of phospholipid can be modified to bind to different ligands, image agents to meet the different delivery requirements.

However, as a popular drug delivery system, liposomes also have their own disadvantages. For example, liposomes often suffer from the problem of instability, which leads to the leakage of drugs during the storage. Furthermore, liposomes have short half-life in blood circulation. The liposomes maybe destabilized by the ions in blood and may lead the leakage to blood stream. Also, liposomes have low solubility and it is hard to remove liposomes from bodies once administrated.

1.5 Phospholipid coated gold nanoparticles

Therefore, we tried to combine the advantages of GNPs with liposomes by forming phospholipid coated GNPs. We proposed that the phospholipid coated GNPs is an ideal drug delivery system in the view of the performance of both liposomes and GNPs. This new system not only provides a nontoxic and stable scaffold for liposomes, but also improves the biocompatibility of GNPs due to the existence of biocompatible phospholipids on their surface. Moreover, phospholipid coated GNPs can improve drug encapsulation efficiency and drug release property of liposomes.

The design of the multifunctional GNPs based nanosystem for diagnostic and therapeutic applications demands a thorough understanding of the uptake mechanism of GNPs to cells. [52] Furthermore, elucidating the uptake mechanism is important for assessing the toxicity of GNPs. For example, it is less likely to cause cellular toxicity or alter the cell function if GNPs do not enter the cells. It is also less prone to kill cells if GNPs are trapped in vesicles and leave cells intact. At last, the study of uptake mechanism is helpful to understand how to maximally

accumulate GNPs in cells, such as tumor cells. It may also benefit the designing of multifunctional and biocompatible GNPs in the future. [28]

Thus, in this study, we investigated the interactions between 30 nm phospholipid coated GNPs with different cell lines (A549 cells, C2C12 cells and C2bbe1 cells). Our main objective is to understand the cellular uptake mechanism in each cell line and to find out what will happen to the GNPs after they enter the cell. [53]

Reference

1. Rosi, N. L., Mirkin, C. A. Nanostructures in Biodiagnostics. *Chem. Rev.*, **2005**, 105, 1547-1562.
2. Kumar, A., Boruah, B. M., Liang, X. J. Gold Nanoparticles: Promising Nanomaterials for the Diagnosis of Cancer and HIV/AIDS. *Journal of Nanomaterials*, **2011**, 2011, Article ID 202187.
3. Vitale, F., Vitaliano, R., Battocchio, C. et al. Synthesis and Microstructural Investigations of Organometallic Pd(II) Thiol-Gold Nanoparticles Hybrids. *Nanoscale Res Lett.*, **2008**, 3, 461-467.
4. Noguez, C. Surface Plasmons on Metal Nanoparticles: The Influence of Shape and Physical Environment. *J. Phys. Chem. C.*, **2007**, 111, 3806-3819.
5. Delehanty, J. B., Boeneman, K., Bradburne, C. E. et al. Peptides for specific intracellular delivery and targeting of nanoparticles: implications for developing nanoparticle-mediated drug delivery. *Therapeutic Delivery*, **2010**, 1, 411-433.
6. Jin, S., Leach, J. C., Ye, K. Nanoparticle-mediated gene delivery. *Methods Mol Biol*., **2009**, 544, 547-57.
7. De Volder, M. F., Tawfick, S. H., Baughman, R. H. et al. Carbon Nanotubes: Present and Future Commercial Applications. *Science*, **2013**, 339, 535-539.

8. Tao, C. N. R., Vivekchand, S. R. C., Govindaraj, A. 1.10 – Inorganic Nanowires. *Comprehensive Nanoscience and Technology*, **2011**, 1, 289-314.
9. Leung, V., Ko, F. Biomedical applications of nanofibers. *Polymers for Advanced Technologies*, **2011**, 22, 350-265.
10. Kinge, S., Crego-Calama, M., Reinhoudt, D. N. Self-Assembling Nanoparticles at Surfaces and Interfaces. *ChemPhysChem*, **2008**, 9, 20-42.
11. Sperling, R. A., Parak, W. J. Surface modification, functionalization and bioconjugation of colloidal inorganic nanoparticles. *Phil. Trans. R. Soc. A*, **2010**, 368, 1333-1383.
12. Faraday, M. Experimental relations of gold (and other metals) to light. *Phil Trans R Soc London*, **1857,** 14, 145-81.
13. Chandler, J., Robinson, N., Whiting, K. Handling false signals in gold-based tests. *IVD Technol.*, **2001,** 7, 34-45.
14. Rubin, P., Levitt, S. H. The response of disseminated reticulum cell sarcoma to the intravenous injection of colloidal radioactive gold. *J Nucl Med.*, **1964**, 5, 581-94.
15. Root, S. W., Andrews, G. A. Knieseley, R. M. et al. The distribution and radiation effects of intravenously administered colloidal Au 198 in man. *Cancer*, **1954**, 7, 856-66.
16. Yeh, Y. C., Creran, B., Rotello, V. M. Gold nanoparticles: preparation, properties, and applications in bionanotechnology. *Nanoscale*, **2012**, 4, 1871-1880.

17. Kelly, K. L., Coronado, E., Zhao, L. L. et al. The optical properties of metal nanoparticles: the influence of size, shape, and dielectric environment. *J Phys Chem B.*, **2003**, 107, 668-77.
18. Stewart, M. E., Anderton, C. R., Thompson, L. B. Nanostructured plasmonic sensors. *Chem Rev.*, **2008**, 108, 494.
19. Rosi, N. L., Mirkin, C. A. Nanostructures in biodiagnostics. *Chem Rev*., **2005**, 105, 1547-62.
20. Hill, H. D., Vega, R. A., Mirkin, C. A. Non-enzymatic detection of bacterial genomic DNA using the bar code assay. *Anal Chem*., **2007**, 79, 9218-23.
21. Dai, Q., Liu, X., Coutts, J. A one-step highly sensitive method for DNA detection using dynamic light scattering. *J Am Chem Soc*., **2008**, 130, 8138-9.
22. Yguerabide, J., Yguerabide, E. E. Resonance light scattering particles as ultrasensitive lable for detection of analytes in a wide range of applications. *J Cell Biochem Suppl.*, **2001**, 37, 71-81.
23. Huang, X., Qian, W., El-Sayed, I. H. The potential use of the enhanced nonlinear properties of gold nanospheres in photothermal cancer therapy. *Lasers Surg Med*., **2007**, 39, 747-53.
24. Huang, X., Jain, P. K., El-Sayed, I. H. et al. Plasmonic photothermal therapy (PPTT) using gold nanoparticles. *Lasers Med Sci*., **2008**, 23, 217-28.

25. Zharov, V. P., Mercer, K. E., Galitovskaya, E. N. et al. Photothermal nanotherapeutics and nanodiagnostics for selective killing of bacteria targeted with gold nanorods. *Biophys J.*, **2006**, 90, 619-27.
26. Templeton, A.C., Wuelfing, W. P., Murray, R. W. Monolayer-protected cluster molecules. *Accounts of Chemical Research*, **1999**, 33, 27-36.
27. Duncan, B., Kim, C., Rotello, V. M. Gold nanoparticle platforms as drug and biomacromolecule delivery systems. *Journal of Controlled Release*, **2010**, 148, 122-127.
28. Chithrani, B. D., Ghazani, A. A., and Chan, W. C. Determining the Size and Shape Dependence of Gold Nanoparticle Uptake into Mammalian Cells. *Nano Letters*, **2006**, 6, 662-8.
29. Connor, E. E., Mwamuka, J., Gole, A. et al. Gold Nanoparticles are Taken up by Human Cells but do not Cause Acute Cytotoxicity. *Small*, **2005**, 1, 325-27.
30. Hauck, T. S., Ghazani, A. A., Chan, W. C. Assessing the Effect of Surface Chemistry on Gold Nanorod Uptake, Toxicity, and Gene Expression in Mammalian Cells. *Small*, **2008**, 4, 153-9.
31. Tkachenko, A., Xie, H., Liu, Y. et al. Cellular Trajectories of Peptide-modified Gold Particle Complexes: Comparison of Nuclear Localization Signals and Peptide Transduction Domains, *Bioconjugate Chem*., **2004**, 15, 482-490.

32. Connor, E., Mwamuka, J., Gole, A. et al. Gold nanoparticles are taken up by human cells but do not cause acute cytotoxicity. *Small*, **2005**, 1, 325-327.

33. Cho, W. S., Cho, M., Jeong, J. Acute toxicity and pharmacokinetics of 13 nm-sized PEG-coated gold nanoparticles. *Toxicology and Applied Pharmacology*, **2009**, 236, 16-24.

34. Pernodet, N., Fang, X., Sun, Y. et al. Adverse effects of citrate/gold nanoparticles on human dermal fibroblasts. *Small*, **2006**, 2, 766-773.

35. Murphy, M.P., Holmgren, A., Larsson, N. G. et al. Unraveling the biological roles of reactive oxygen species. *Cell Metab*., **2011**, 13, 361-366.

36. Pan, Y., Leifert, A., Ruau, D. et al. Gold Nanoparticles of Diameter 1.4 nm Trigger Necrosis by Oxidative Stress and Mitochondrial Damage. *Small*, **2009**, 5, 2067-2076.

37. Du, L., Miao, X., Jia, H. Detection of nitric oxide in macrophage cells for the assessment of the cytotoxicity of gold nanoparticles. *Talanta*, **2012**, 101, 11-16.

38. Roa, W., Zhang, Z., Guo, L. Gold nanoparticle sensitize radiotherapy of prostate cancer cells by regulation of the cell cycle. *Nanotechnology*, **2009**, 20, 37-51

39. Born, P. J., Muller-Schulte, D. Nanoparticles in Drug Delivery and Environmental Exposure: Same Size, Same Risks? *Nanomedicine*, **2006**, 1, 235-49.

40. Vijayakumar, S., Ganesan, S. Size-dependent in vitro cytotoxicity assay of gold nanoparticles. *Toxicological & Environmental Chemistry*, **2013**, 95, 277-287.
41. Freese, C., Uboldi, C., Gibson, M. I. et al. Uptake and cytotoxicity of citrate-coated gold nanospheres: Comparative studies on human endothelial and epithelial cells. *Particle and Fibre Toxicolog,* **2012**, 9, 23.
42. Ng, K. C., Cheng, W. L. Fine-tuning longitudinal plasmon resonances of nanorods by thermal reshaping in aqueous media. *Nanotechnology,* **2012**, 23, 105602.
43. Tarantola, M., Pietuch, A., Schneider, D. et al. Toxicity of gold-nanoparticles: Synergistic effects of shape and surface functionalization on micromotility of epithelial cells, *Nanotoxicology*, **2011**, 5, 254-268.
44. Alkilany, A. M., Nagaria, P. K., Hexel, C. R. et al. Cellular uptake and cytotoxicity of gold nanorods: molecular origin of cytotoxicity and surface effects. *Small*, **2009**, 6, 701-8.
45. Dong, P., Wang, X., Gu, Y. et al. Self-assembled biodegradable micelles based on star-shaped PCL-b-PEG copolymers for chemotherapeutic drug delivery. *Colloids and Surfaces A: Physicochemical and Engineering Aspects*, **2010**, 358, 128-134.
46. Bitounis, D., Fanciullino, R., Iliadis, A. et al. Optimizing druggability through liposomal formulations: new approaches to an old concept. *ISRN Pharm*., **2012**, 2012, 738432.

47. Immordino, M. L., Dosio, F., Cattel, L. Stealth liposomes: review of the basic science, rationale, and clinical applications, existing and potential. *Int J Nanomedicine*, **2006**, 1, 297-315.
48. Veerareddy, P. R., Vobalaboina, V. Review Lipid-based formulations of amphotericin B. *Drugs Today (Barc)*, **2004**, 40, 33-45.
49. Allen, T. M., Martin, F. J. Review Advantages of liposomal delivery systems for anthracyclines. *Semin Oncol*., **2004**, 6 Suppl 13, 5-15.
50. Alberts, D. S., Muggia, F. M., Carmichael, J. et al. Review Efficacy and safety of liposomal anthracyclines in phase I/II clinical trials. *Semin Oncol*., **2004**, 6 Suppl 13, 53-90.
51. Torchilin, V. P. Recent advances with liposomes as pharmaceutical carriers. *Nature Reviews*, **2005**, 4, 145-160.
52. Chithrani, B. D., Chan, W. C. W. Elucidating the Mechanism of Cellular Uptake and Removal of Protein-Coated Gold Nanoparticles of Different Sizes and Shapes. *Nano Lett.*, **2007**, 7, 1542-1550.
53. Nativo, P., Prior, I. A., Brust, M. Uptake and Intracellular Fate of Surface-Modified Gold Nanoparticles. *ACS Nano*, **2008**, 2, 1639-1644.

Chapter 2 Synthesis and characterization of SOPG coated GNPs

2.1 Synthesis of gold nanoparticles

GNPs have attracted great scientific interest because of their various applications. [1-3] The synthesis of GNPs can be made either by vacuum evaporation or colloid chemistry. In the vacuum evaporation, a thin film of metal is deposited on a substrate and evaporated in vacuum chamber. [4, 5] Generally, in the colloid chemistry, GNPs are generated by the reduction of chloroauric acid ($HAuCl_4$) or chloroauric salt ($KAuCl_4$). [6] As shown in Figure 2.1 (A), the first step is the rapid reduction of gold precursor ion to gold atoms that form primary nuclei, which takes less than 200 ms. In the second step, the solution becomes supersaturated as more and more gold atoms are formed. Then gold atoms start to grow to bigger particles driven mainly by the force of coalescence shown in Figure 2.1 (B). The rest of gold particles will grow on the top of existing particles. The GNPs will be uniform in size if the solution is stirred vigorously.

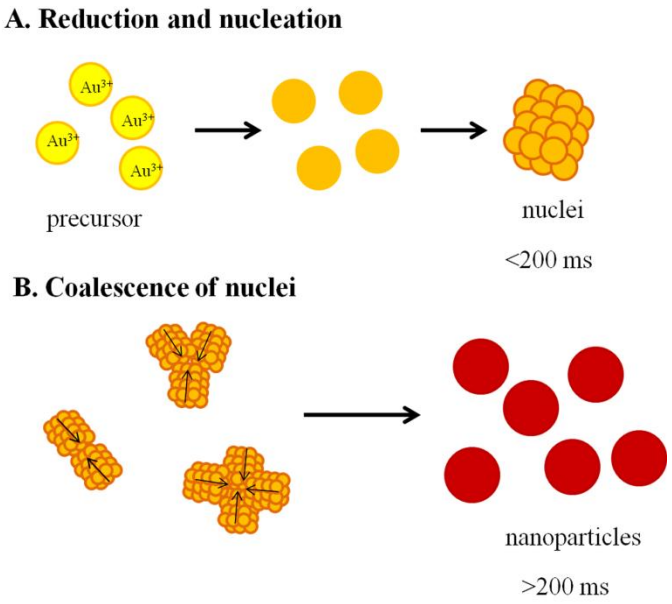

Figure 2.1. Schematic illustration of the formation process of GNPs. (A) The first step is the reduction and nucleation, which takes less than 200 ms. (B) In the second step, nuclei collapse to bigger nanoparticles because of the coalescence, which takes longer time. [Adapted from reference 6]

To prevent the aggregation of larger particles, capping agents or stabilizing agents have to be used. The GNPs can be stabilized by different ligands, such as organic compounds, DNA, peptides and proteins. For example, in the synthesis of citrate stabilized GNPs, citrate ions act as both reducing agent and stabilizing agent (capping agent). There are several important methods to make the GNPs using colloid chemistry.

Turkevich method

The Turkevich method is the simplest synthesis method available. It was developed by J. Turkevich et al. in 1951 and improved by G. Frens in the 1970s. [7, 8] The method involves the reduction of boiling precursor gold ions to GNPs

by sodium citrate. It is usually used to generate the monodisperse spherical GNPs with size around 10-20 nm. It is possible to make bigger GNPs by decreasing the amount of citrate at the expense of monodispersity and uniformity in shape. Recently, extensive studies suggest gold nanowires are formed in the process, causing the dark color of the reaction before it turns to ruby color. [9]

Brust method

The Brust method is used to synthesize GNPs in a two phase system. It was developed by Brust and Schiffrin in the early 1990s. [10] This method is used to produce GNPs in organic solvents that are immiscible with water (for example, toluene). Usually, Tetraoctylammonium bromide (TOAB) is used to act as a phase transfer catalyst and a stabilizing agent, and sodium borohydride is used as the reducing agent. The size of GNPs from this method will be 2 to 6 nm. [11]

In this reaction, the TOAB does not stick strongly to the surface of the GNPs. So the stability of the GNPs in solution is poor and they will aggregate slowly over approximately two weeks. In order to prevent the aggregation, it is important to add stronger binding agents, such as thiols, to form a stronger covalent bond with the GNPs. Alkanethiol stabilized GNPs can be centrifuged to remove supernatant and be redissolved in solution. Some of the phase transfer catalyst may affect the physical properties of GNPs if it remains bound to the surface of the GNPs after purification.

Martin Method

The Martin method was discovered by Eah in 2010. This method generates “naked” GNPs in water by the reduction of precursor gold ions. The naked GNPs

are stabled dispersed in water even without the presence of stabilizing agents. The GNPs from this method are nearly monodisperse and size can be tuned from 3.2 to 5.2 nm precisely and reproducibly. [12] The point of stabilizing the solution is to ensure the stability of the $HAuCl_4$ by HCl for a few month and $NaBH_4$ by NaOH for hours respectively.

The “naked” GNPs are stabilized by a monolayer of 1-dodecanethiol. And then it was mixed with a mixture of water, acetone and hexane to make the phase transfer to hexane. This method doesn’t need the purification step because all of the by-products remain in the water acetone phase. This new synthesis is easy, cheap and green by combing advantages of Turkevich method and Brust method.

2.2 Synthesis of phospholipid coated gold nanoparticles

The GNPs themselves have low affinity for cells and much work has focused on coating a biocompatible layer on the surface of GNPs to promote their interactions with cells. [13, 14] Liposomes, which are made of phospholipid bilayers, have also been extensively studied as drug delivery system because of their biocompatibility. [15, 16] Furthermore, phospholipids are integral components of cell membranes. They are composed of polar head groups and nonpolar hydrocarbon tails. It is possible to modulate the biomolecular interaction by changing the hydrophobic and hydrophilic components of the phospholipids. Hence, we can make a various biocompatible nanomaterials by using the phospholipids as capping reagents for GNPs. [17]

Furthermore, the optical properties of gold nanoparticle sensor can be modified because the phospholipid can modulate the dielectric properties of GNPs. [18]

The interaction between GNPs and phospholipid can be adjusted by changing the nature of phospholipid head group. The number and size of hydrocarbon tails can be changed to modulate the dimension and kinetics to form the lipid coated nanoparticles. Additionally, various phospholipids can be mixed together to alter the properties of the integrated architecture. [19] Due to the intrinsic amphiphilic characteristics, the lipid coated GNPs can be fabricated to substrates with different polarities.

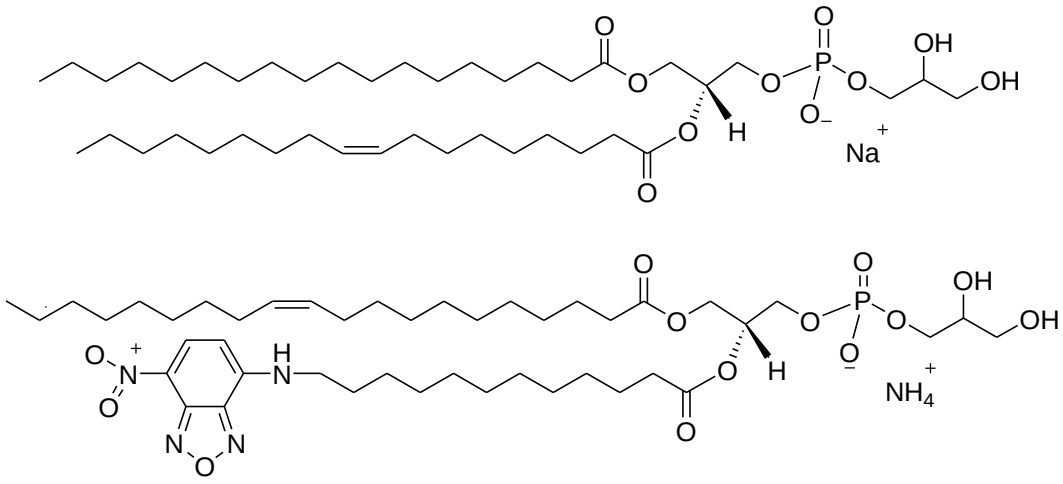

Figure 2.2. Structure of 1-stearoyl-2-oleoyl-*sn*-glycero-3-phospho-(1'-*rac*-glycerol) (SOPG) and 1-oleoyl-2-{12-[(7-nitro-2-1,3-benzoxadiazol-4-yl)amino] dodecanoyl}-*sn*-glycero-3-[phospho-*rac*-(1-glycerol)] (NBD labeled PG or NBD-PG).

Here we report the synthesis of GNPs capped by SOPG (1-stearoyl-2-oleoyl-*sn*-glycero-3-phospho-(1'-*rac*-glycerol)), a phospholipid with a negative charge at the head and two hydrophobic tails of 18 carbons each (Figure 2.2), one saturated and one with a single double bond. In order to use fluorescence as a means of tracking

the GNPs in live cells, we introduced a small amount of 7-nitro-2-1,3-benzoxadiazol-4-yl (NBD) labeled PG into the SOPG bilayer.

2.3 Experiment

2.3.1 Materials

Tetrachloroauric acid ($HAuCl_4$) was bought from Strem Chemicals, Inc. Trisodium citrate (Na_3Cit) was obtained from Sigma-Aldrich. Sodium borohydride ($NaBH_4$) was purchased from EMD Millipore, and ascorbic acid (AA) ($C_6H_8O_6$) was obtained from EM Science, Div EM Industries Inc. The lipids 1-stearoyl-2-oleoyl-*sn*-glycero-3-phospho-(1'-*rac*-glycerol) (sodium salt) (SOPG) (18:0-18:1), 1-oleoyl-2-{12-[(7-nitro-2-1,3-benzoxadiazol-4-yl)amino]dodecanoyl} -*sn*-glycero-3-[phospho-*rac*-(1-glycerol)] (ammonium salt) (NBD-PG) (18:1-12:0) were purchased from Avanti Polar Lipids. MilliQ water was used for the synthesis of GNPs.

2.3.2 Synthesis of NBD labeled SOPG coated gold nanoparticles (NBD-SOPG-GNPs).

The NBD-SOPG-GNPs were synthesized by the seed-mediated methods [20] Firstly, the seed solution was made by mixing $HAuCl_4$ solution and trisodium citrate solution. And then sodium borohydride solution was added to reduce the precursor gold ions to GNPs. The seeds formed in this solution are about 2-5 nm in size. The growth solution is made from a $HAuCl_4$ solution containing SOPG and NBD-PG. Fresh seed solution was added to the growth solution and stirred for a while. Then the weak reducing agent ascorbic acid was added to reduce the precursor gold ions in the presence of the seeds. The mixture was mixed and then

stored in the fridge (at 4 °C) overnight. By changing the concentration and reaction time, we are able to get NBD-SOPG-GNPs with different size and shape.

2.4 Characterization of gold nanoparticles

The synthesized NBD-SOPG-GNPs were characterized by UV-Visible (UV-Vis) spectroscopy, dynamic light scattering (DLS), zeta potential and electron microscopy (EM).

2.4.1 UV-Visible spectroscopy

The surface plasmon resonance of GNPs depends on the size, shape and state of aggregation of GNPs. [21, 22] UV−visible spectroscopy is a very useful technique to estimate the size, concentration and aggregation level of GNPs. Table 2.1 illustrates the influence of GNPs size on the surface plasmon resonance. The absorption maximum (lambda max) red shifts from 517 nm to 575 nm when the size of GNPs changes from 8.9 nm to 99.3 nm.

Diameter, nm	**λ max**
8.9 nm	517
14.8 nm	520
21.7 nm	521
48.3 nm	533
99.3 nm	575

Table 2.1. The maxima absorption of GNPs red shifts to higher wavelength when the size increases. [Adapted from reference 23]

2.4.2 Dynamic light scattering

Dynamic light scattering, or photon correlation spectroscopy, is a useful technique to determine the size distribution of particles in suspension. [24] When the light hits the particles, the incident light is scattered in all directions when the particles are small enough to be comparable to the wavelength of light (below 250 nm). Figure 2.3 shows the intensity of scattered light fluctuates as a function of time. [25] The intensity of the scattered light at various angles depends on the relative position of particles in solution. The scattered light interacts with surrounding particles either in constructive or destructive way. When the particles move, the intensity of scattered light fluctuate at a time scale depends on the diffusion rate of the particles. The fluctuation of scattered light is therefore used to determine diffusion time, from which the size of particles can be extracted. Dynamic light scattering requires fairly high concentration. If it is too diluted, the interference of scattered light with neighbouring particles will be weak.

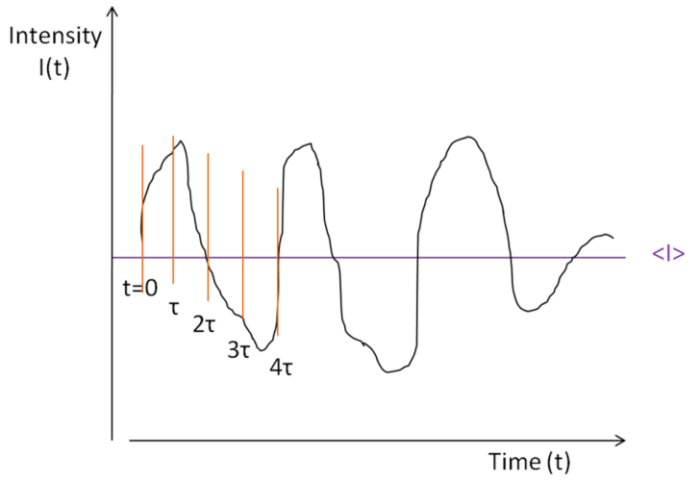

Figure 2.3. The intensity of scattered light fluctuates as a function of time. After the completion of one cycle, the time grid shifts to next channel and cycle is repeated. [Adapted from reference 26]

The dynamic information of particles will be extracted from an autocorrelation function of the intensity of scattered light. The autocorrelation function is derived from the intensity fluctuation as follows:

$$g^2(\tau) = \frac{\langle I(t)I(t+\tau)\rangle}{\langle I(t)\rangle^2}$$

where $g^2(\tau)$ is the autocorrelation function, τ is delay time, and <I(t)> is the mean intensity.

After a very short time interval, the similarities or correlation is high because the particles do not have enough time to move far away from its initial state. After a long time period, the correlation function will decay exponentially, which means there will be no similarities between the initial and final states. The exponential decay of autocorrelation function is related to the diffusion time of particles, from which the diffusion coefficient can be extracted by:

$$\tau_D = \frac{\omega_1^2}{2nD}$$

Where ω_1 is the radius of the volume element in XY direction and n is the number of dimensions.

The mean radius of particles will then be obtained by the Stokes-Einstein equation:

$$R = \frac{k_B T}{6\pi\eta D}$$

where k_B is the Boltzmann constant, T is the temperature in Kelvin scale, and η is the viscosity of solvent.

It is essential to note that the size obtained from dynamic light scattering is the hydrodynamic radius of the particles, which includes the ions, solvents and other molecules that move with the particles. [27] Furthermore, the size determined by DLS is the radius of sphere. For example, if the scatter is a nanorod with aspect ratio of 1:2, the determined size is not same to the width or length of the nanorod.

2.4.3 Zeta potential

Zeta potential is an intrinsic property of particles in suspension, and usually denoted by the Greek letter zeta, hence ζ-potential. The zeta potential is the electric potential difference between the slipping layer and the bulk fluid that is far away from the interface layer. (Figure 2.4) [28-29]

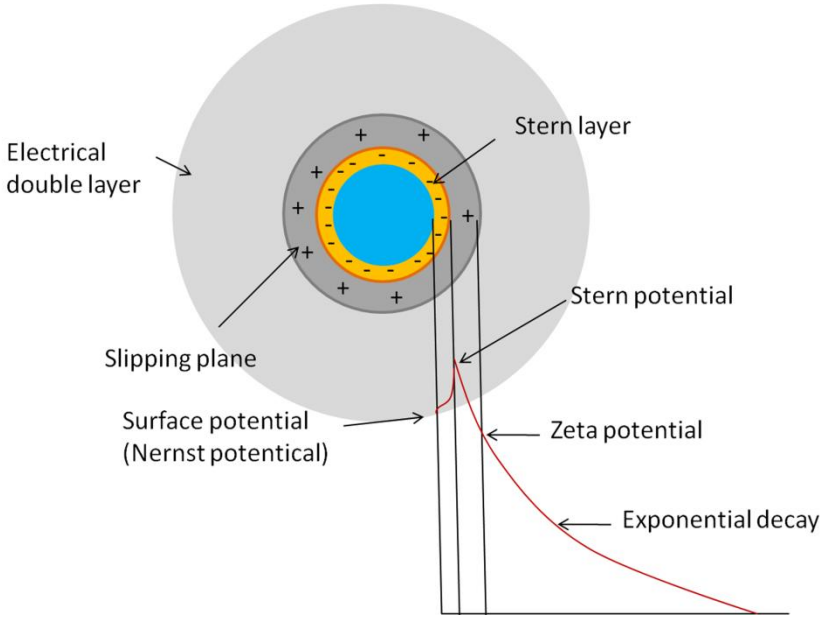

Figure 2.4. Diagram describes a particle with a negative zeta potential. The first layer composed of negative charge is called stern layer. The measured zeta potential is the electrical potential difference between the slipping layer and the bulk medium. [Adapted from reference 30]

The significance of the zeta potential is that it can be used to determine the stability of the colloidal suspension, such as GNPs solution. The zeta potential is electrical potential of particles and reveals the scale of repulsion of particles in dispersion. The particle solution with high zeta potential will have better stability because it has high degree of repulsion and thus resists aggregation. When the zeta potential gets low, the attraction of particles will exceed the repulsion force and cause the aggregation. Thus, particle suspension will be electrically stabilized when it possess high zeta potential (positive or negative) and tend to aggregate when it has low zeta potential. [31, 32]

2.4.4 Electron microscope

An electron microscope is a form of microscope that illuminates sample by an electron source. An EM has greater resolution than a light microscope as the wavelength of electron is about 100,000 times shorter than the light. Generally, there are two types of electron microscope: Scanning Electron Microscope (SEM) and Transmission Electron Microscope (TEM). [33, 34]

Scanning Electron Microscopes (SEM)

SEM produces images by scanning across the sample with a focused beam of electrons. The incoming electrons interact with the electrons of the sample with carbon coating to produce various signals that indicate the information of sample surface and composition. These various signals include back scattered electrons, secondary electrons (SE), X-rays and transmitted electrons. Usually, all of the SEMs are equipped with the secondary electrons detectors, but it is rare to find a single SEM machine to be supplied with detectors for all possible signals. In the secondary electron imaging (SEI), the SEM can produce resolution better than 1 nm to show the details of a sample surface. [35] Due to the very sharp electron beam, the SEM can achieve high depth of field and produce a characteristics three dimensional images for the surface structure of sample.

Transmission Electron Microscope (TEM)

In the TEM, a beam of electrons interact with the electrons of sample when it transmits through an ultrathin specimen (less than 100 nm). The most common operation mode of TEM is bright field mode, in which the TEM image contrast is due to absorption and scattering of electrons by the sample. Usually, materials

have higher atomic number or deeper thickness will appear dark, while regions with less or no sample will shows brighter. [36] It is often necessary to enhance the contrast of organic materials by heavy metals in biological specimen because of their low contrast. The beam source of TEM can be a tungsten filament or lanthanum hexaboride (LaB_6). By connecting the electron gun to high voltage source, the gun will have enough current to emit electrons into vacuum either by thermoionic or field electron emission. The accelerated electrons in vacuum are then focused by condenser aperture and objective aperture to specimen. The transmitted electrons from specimen are then focused on fluorescent screen to be detected by a CCD camera to produce an image. Electron microscope has been widely used for the imaging of GNPs because of its high resolution.

Electron diffraction

Wave-particle duality states that the behaviour of electron can be described as a wave function. Electron diffraction is similar to X-ray or neutron diffraction and related to the wave property of electron. Electron diffractions are often used in the solid state physics to analyze the crystal structure of solid. Electron diffraction experiments are usually carried out in a TEM machine, in which electrons are accelerated by a powerful voltage to gain desired energy. The wavelength of electron can be obtained by the Broglie relationship:

$$\lambda = \frac{h}{p} \quad (1)$$

where h is Planck's constant and p is the momentum of electron. λ is called the de Broglie wavelength.

The accelerating energy of electron can be measured by:

$$\frac{1}{2}mv^2 = eV \text{ or } p = mv = \sqrt{2meV} \quad (2)$$

where v is the velocity of electrons after accelerated by a voltage potential V.

Substituting the de Broglie relationship, equation (1) is

$$\lambda = \frac{h}{p} = \frac{h}{\sqrt{2meV}}$$

The wavelength of electrons can be determined when the values of m and e are known. [37, 38]

BRAGG'S LAW

The electromagnetic wave that are scattered by crystal lattice will cause diffraction pattern which is similar to the case of diffraction grating. For a crystal, the waves scattered by lattice planes are separated by the distance of plane d. The scattered waves will interfere constructively when the path length difference of each wave is equal to the integer multiple of the wavelength (Figure 2.5). The path length difference of two constructive waves is described by 2dsinθ, where θ is the scattering angle. Bragg's Law is used to determine this constructive interference from a crystalline lattice.

$$2d \sin\theta = n\lambda$$

where n is an integer, d is the distance of crystallian plane, and λ is wavelength of incident light.

For a cubic crystal, the distance between two parallel planes is given by:

$$d = \frac{a}{\sqrt{H^2 + K^2 + L^2}}$$

where H, K, L are the Miller indices and a is the length of the crystal cube.

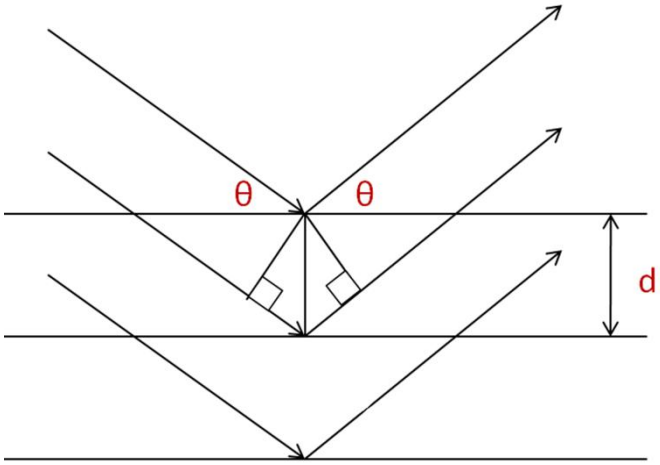

Figure 2.5. Bragg diffraction. A beam approaches a crystalline solid and is scattered by two different atoms. One of the scattered lights travels an extra length of 2dsinθ by comparing to the other scattered light. The two scattered lights will have constructive interference when the extra length 2dsinθ is equal to $n\lambda$. [Adapted from reference 39]

2.5 Synthesis and characterization of 30 nm NBD-SOPG-GNPs

2.5.1 Synthesis of 30 nm NBD-SOPG-GNPs

The NBD-SOPG-GNPs were synthesized by the seed-mediated methods. [20] First, the seed solution was made by mixing 30 mL $HAuCl_4$ solution (0.72 mM) and 10 mL trisodium citrate solution (3.79 mM). After stirring for 10 min, 3 mL sodium borohydride solution (2.91 mM) was added and the mixture was stirred for another 5 min. The seeds formed in this solution are about 2-3 nm in size measured by dynamic light scattering. The growth solution is made from a $HAuCl_4$ (0.54 mM, 13 mL) solution containing SOPG (1.11 mM) with 8.77% (w/w) NBD labeled PG (NBD-PG). Fresh seed solution (0.3 mL) was added to the growth solution and stirred for 8 min. Then 0.25 mL ascorbic acid (8.97 mM) was

added. The mixture was stirred for 25 min and then stored in the fridge (at 4 °C) overnight. This process reproducibly produced 30 nm NBD-SOPG-GNPs.

2.5.2 Characterization of 30 nm NBD-SOPG-GNPs

The absorption spectrum of the NBD-SOPG-GNPs was measured in water using an Agilent 8453 UV-Vis spectrophotometer. Figure 2.6 shows the UV-visible spectrum of NBD-SOPG-GNPs with two absorption bands at 473 nm and 530 nm respectively. The peak at 530 nm corresponds to the absorption of the surface plasmon resonance of GNPs, which is created on the edge of the metal particle with the absorption depending on the size and shape of nanoparticles. The peak at 473 nm arises from the absorption of NBD dye.

Usually, a 30 nm citrate coated GNPs will have maxima absorption at 525-526 nm. However, our 30 nm NBD-SOPG-GNPs has a 4 nm redshift comparing to the citrate coated GNPs. At 1996, Liz-Marzan, Giersig, and Mulvaney calculated the influence of the silica layer on the optical properties of GNPs suspension. [40] They found a 4 nm redshift at the position of the absorption maximum when the shell thickness increased. The suggested that the redshift is because of the increase of the local refractive index around the particles. The phospholipid bilayer has a similar refractive index to silica at 1.456, which probably cause the GNPs to have a 4 nm shift at the maximum absorption by the same effect. [40]

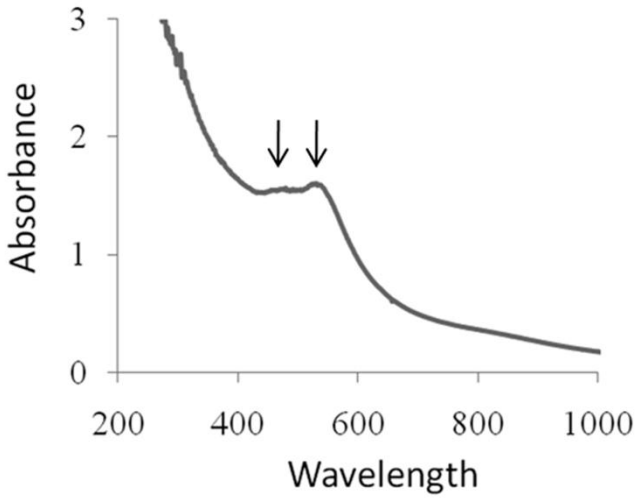

Figure 2.6. The UV-Vis absorption spectrum of 30 nm NBD-SOPG-GNPs shows two absorption bands at 473 nm and 530 nm.

The size of synthesized NBD-SOPG-GNPs was measured in water by Malvern Nano-S Dynamic Light Scattering. The dynamic light scattering provides an estimate of the size distribution by number as shown in Figure 2.7. The size distribution by number shows the NBD-SOPG-GNPs is about 26 nm with a distribution width of 5 nm. The size distribution by intensity shows a distribution of 29 ± 6 nm, which is more consistent with the results from electron microscopy. (Data not shown) For our preparations we can reproducibly obtain this narrow size distribution of NBD-SOPG-GNPs.

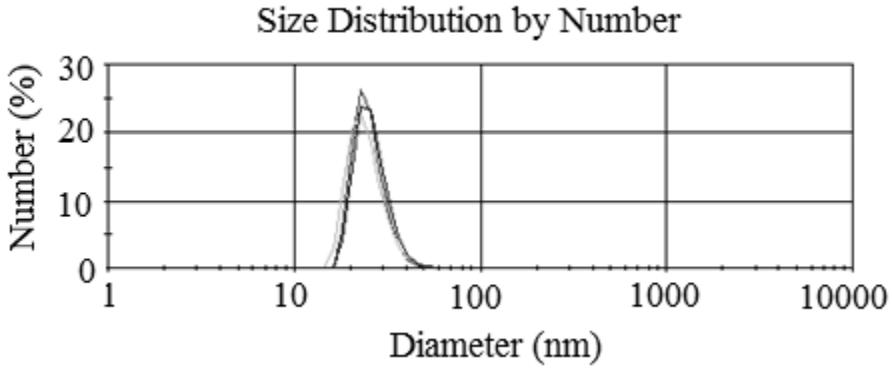

Figure 2.7. The dynamic light scattering shows the synthesized NBD-SOPG-GNPs with a size distribution of 26 ± 5 nm.

The Zeta potential of NBD-SOPG-GNPs was measured by Malvern Zetasizer particle size analyser. The Zeta potential of 30 nm NBD-SOPG-GNPs was very negative and measured as -65 mV in water (Figure 2.8). This -65 mV electrical potential suggested that the 30 nm NBD-SOPG-GNPs colloid solution should be very stable – which is also observed. The phospholipid SOPG has a negative charge head and oriented itself to form a bilayer on the surface of the particles with the negative head toward the water, and the carbon lipophilic tail toward the center of bilayer. Thus, the existence of phospholipid SOPG aided the formation of stable GNPs and contributed to the negative charge of the GNPs.

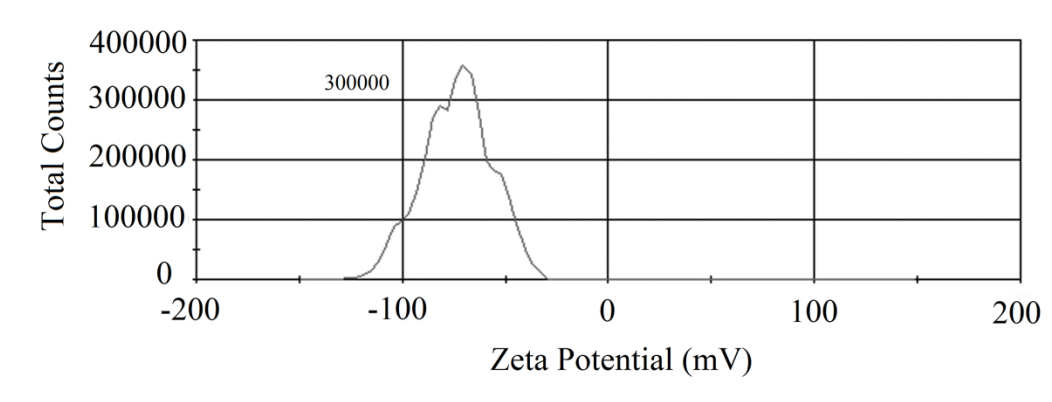

Figure 2.8. The Zeta potential of 30 nm NBD-SOPG-GNPs was measured by Malvern Zetasizer particle size analyzers in water.

Ivanov et al. shows the citrate coated GNPs with size at 13.3 nm has a zeta potential of −39.7 ± 0.7 mV. The SOPG phospholipid has a similar negative charge as the citrate and thus provides a negative charge to the GNPs. This is also an indirect evidence to prove that the SOPG phospholipids form a lipid bilayer and face their negative charge heads toward the water. [41]

The TEM and SEM images of GNPs were taken by TEM/STEM - JEOL 2200FS and Scanning Electron Microscope - Field emission S-4800 respectively. As showed in Figure 2.9, the NBD-SOPG-GNPS show ordered crystal structures in the TEM images. The TEM image also shows that a number of GNPs with clearly defined hexagonal contours but with overall near-spherical geometry with an average diameter of about 30 ± 4 nm [measured from a number of images with hundreds of particles], consistent with the DLS distribution. The SEM image in Figure 2.10 shows the NBD-SOPG-GNPs are very uniform in size and are clearly separated from each other without aggregation.

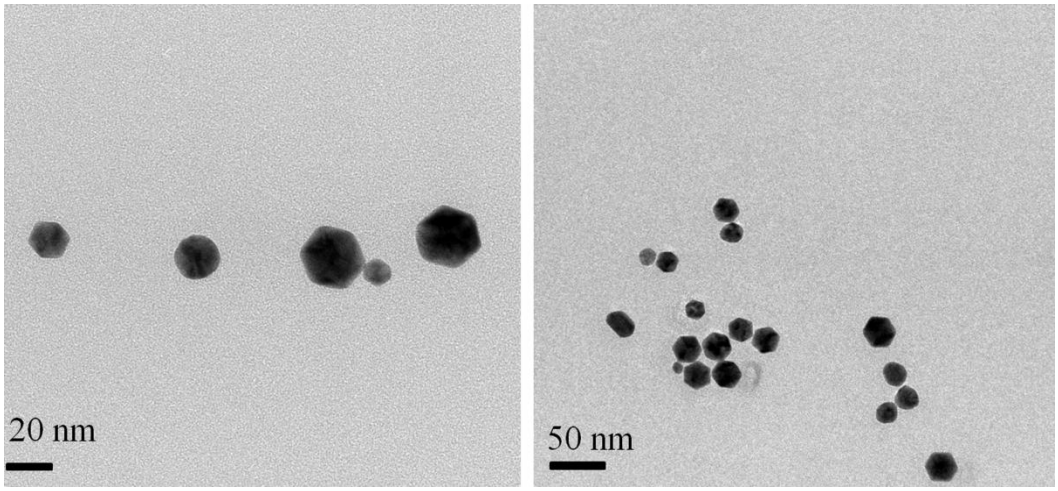

Figure 2.9. TEM images of 30 nm NBD-SOPG-GNPs taken by TEM/STEM - JEOL 2200FS.

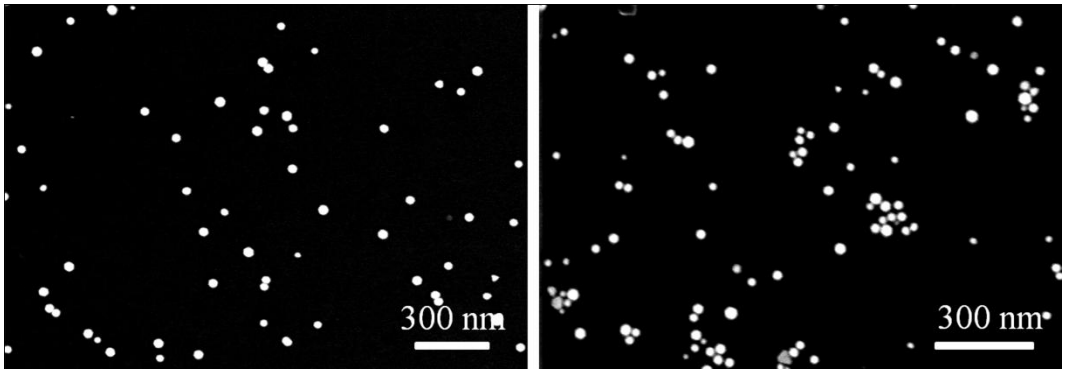

Figure 2.10. SEM images of 30 nm NBD-SOPG-GNPs taken by Scanning Electron Microscope - Field emission S-4800.

2.5.3 Characterization of phospholipid bilayer on the surface of GNPs

As showed in the Figure 2.8, the NBD-SOPG-GNPs have a negative zeta potential at -65 mV. Thus, we propose the SOPG phospholipid forms a bilayer on the surface of GNPs to make its negative charged head toward water and carbon tail points to the bilayer wall. In order to prove the existence of this bilayer, we tried to use the higher resolution – transmission electron microscope to characterize the bilayer of GNPs. As the phospholipid has different atomic

number to the gold, the phospholipid bilayer will have weaker contrast relative to the GNPs. In order to enhance the contrast of lipid bilayer, we stained the specimen with uranyl acetate. As showed in the Figure 2.11 (A), it is obvious that the GNPs is surrounded by a 2-4 nm layer, which is compatible with the thickness of a phospholipid bilayer. Furthermore, we found that this phospholipid bilayer is quite stable on the surface of GNPs and doesn't fuse with the cell membrane as shown in Figure 2.11 (B). In this experiment, the cell membrane was stained by lipophilic dye DiI with red color. Thus, we confirmed the existence of the phsopholipid bilayer which sticks to the surface of GNPs and does not diffuse to cell membrane. And it is probably that this phospholipid bilayer causes the GNPs to have 4 nm redshift by changing the local refrective index around the GNPs. [39]

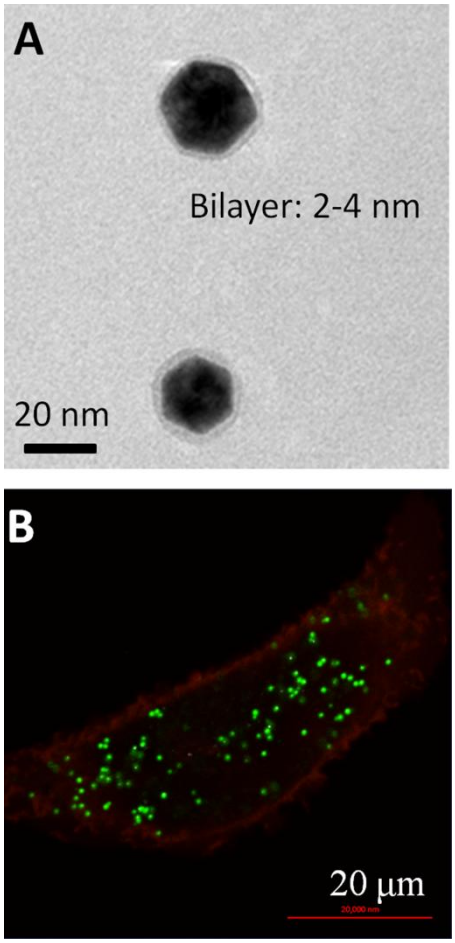

Figure 2.11. The TEM image shows the bilayer of GNPs is about 2-4 nm (A). The fluorescence image shows that the NBD-SOPG-GNPs (green) do not fuse with cell membrane which is stained by DiI red (B).

2.6 Synthesis and characterization of 30-50 nm NBD-SOPG-GNPs

2.6.1 Synthesis of 30-50 nm NBD-SOPG-GNPs

The 30-50 nm NBD-SOPG-GNPs were synthesized by a three steps seed-mediated methods. [20] In the first step, the seed 1 solution was made by mixing 22.5 mL $HAuCl_4$ solution (0.72 mM) and 7.5 mL trisodium citrate solution (3.79 mM). After stirring for 10 min, 3 mL sodium borohydride solution (2.91 mM) was added and the mixture was stirred for another 5 min. The seeds formed in the

first step is ruby red and seeds are about 2-3 nm in size measured by dynamic light scattering. In the second step, seed 2 solution was made by mixing 7.5 mL $HAuCl_4$ solution (0.72 mM) with 2.5 mL trisodium citrate solution (3.79 mM). Then 0.2 mL seed 1 solution was added and reaction was stirred for further 5 min. A weak reducing agent ascorbic acid (0.2 mL, 8.97 mM) was then added and stirred for 10 min. In the last step, the growth solution is mixed by $HAuCl_4$ (0.54 mM, 13 mL) solution containing SOPG (1.11 mM) with 8.77% (w/w) NBD-PG. Fresh seed 2 solution (0.1 mL) was added to the growth solution and stirred for 8 min. Then 0.1 mL ascorbic acid (8.97 mM) was added. The mixture was stirred for 25 min and then stored in the fridge (at 4 °C) overnight. This process reproducibly produced 30-50 nm NBD-SOPG-GNPs.

2.6.2 Characterization of 30-50 nm NBD-SOPG-GNPs

The absorption spectrum of 30-50 nm NBD-SOPG-GNPs was measured in water using Agilent 8453 UV-vis Spectrophotometer. Figure 2.12 shows the UV-vis spectrum of 30-50 nm NBD-SOPG-GNPs with an absorption peak at 534 nm. This peak corresponds to the absorption of the surface plasmon resonance of GNPs at size of 30-50 nm with a 4 nm phospholipid coating.

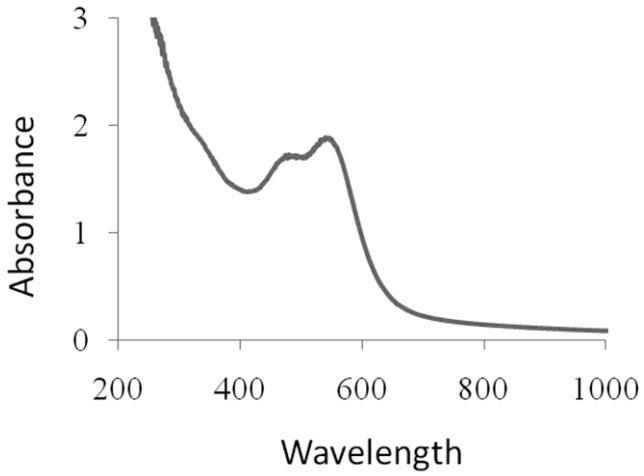

Figure 2.12. The UV-vis absorption spectrum of 30-50 nm NBD-SOPG-GNPs shows an absorption band at 534 nm.

The size of NBD-SOPG-GNPs made by this synthesis method was measured in water by Malvern Nano-S Dynamic Light Scattering. The dynamic light scattering provides an estimate of the size distribution by number as shown in Figure 2.13. It shows a size distribution of 42 nm with a width of 15 nm.

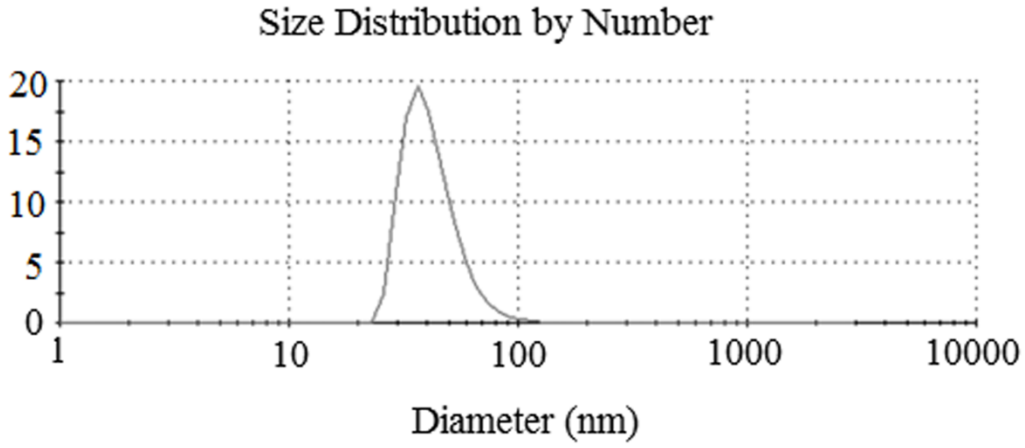

Figure 2.13. The dynamic light scattering shows the synthesized NBD-SOPG-GNPs with a size distribution of 42 ± 15 nm.

The Zeta potential of 30-50 nm NBD-SOPG-GNPs was measured by Malvern Zetasizer particle size analysers. Zeta potential of 30-50 nm NBD-SOPG-GNPs was also very negative and shows similar electrical potential as the 30 nm NBD-SOPG-GNPs at -65 mV. (Figure 2.14). This data suggests that the 30-50 nm NBD-SOPG-GNPs solution are very stable.

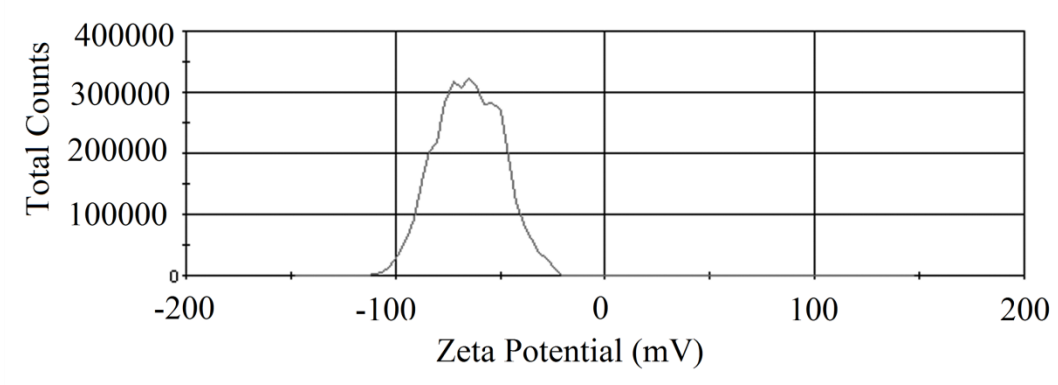

Figure 2.14. The Zeta potential of 30-50 nm NBD-SOPG-GNPs was measured in water.

The SEM image of this synthesize GNPs was taken by Scanning Electron Microscope - Field emission S-4800. As showed in figure 2.15, some of the GNPs show ordered crystal structures with hexagonal or pentagonal structure, but most of them are nearly spherical. These images also show that the GNPs are quite uniform in size and has an average diameter of about 30-50 nm, which is consistent with the DLS distribution.

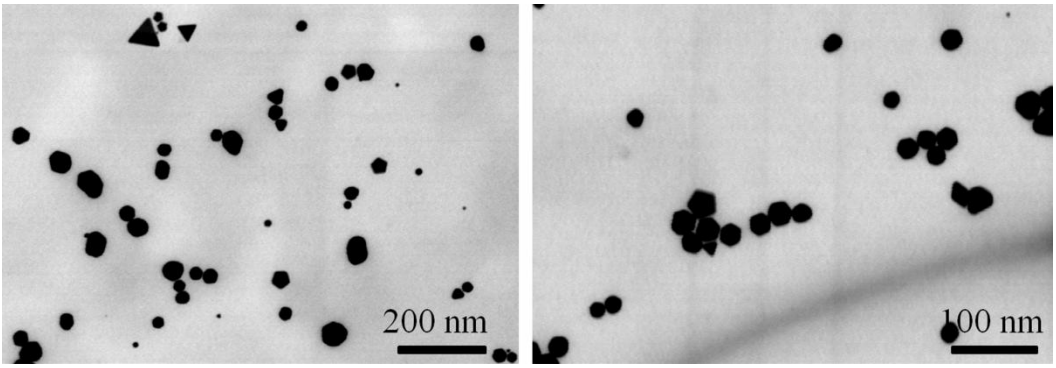

Figure 2.15. Images of 30-50 nm NBD-SOPG-GNPs taken by Scanning electron microscope at transmission mode.

2.6.3 Gold structure confirmed by electron diffraction in TEM

A diffraction pattern was gained by measuring the intensity of scattered waves based on the scattering angle. Figure 2.16 (A) shows the diffraction pattern of the 30-50 nm NBD-SOPG-GNPs from the whole images, which was done by Dr. Jian Chen from National Institute for Nanotechnology (NINT). Figure 2.16 (B) is the simulation of the diffraction pattern obtained by the software Desktop Microscopist (DM).

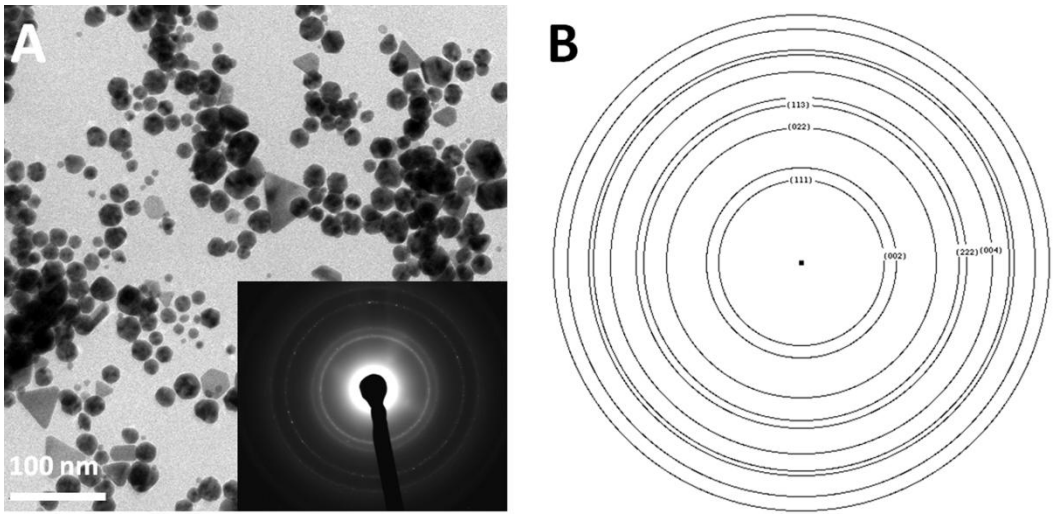

Figure 2.16. (A) shows the bright field (BF) image of NBD-SOPG-GNPs. The inset at low right in the image is the diffraction ring pattern obtained from the whole area shown in image. (B) The simulation was obtained by the software Desktop Microscopist (DM).

Table 2.2. The calculated plane distance d vs. theoretical plane distance of gold crystal.

h k l	**d_{hkl} theo (Å)**	**Exp d (Å)**
1 1 1	2.3549	d_1 = 2.3580
0 0 2	2.0394	d_2 = 2.0394
0 2 2	1.4421	d_3 = 1.4420
1 1 3	1.2298	d_4 = 1.2298

As showed in table 2.2, the first four rings of diffraction pattern are calculated. The calculated plane lengths d match exactly with the theoretical d of gold crystal

at the planes of [111], [002], [022], and [113]. Thus, we concluded that the NPs in the image are crystalline gold nanoparticles.

2.7 Synthesis and characterization of NBD labeled SOPG coated gold nanocubes

2.7.1 Synthesis of NBD labeled SOPG coated gold nanocubes

The SOPG coated gold nanoparticles were synthesized by two step seed-mediated methods. [20] First, the seed solution was made by mixing 20 mL $HAuCl_4$ solution (1.147 mM) and 10 mL trisodium citrate solution (4.3 mM). The solution was stirred for 10 min at room temperature (RT) and then 15 mL sodium borohydride solution (6.3 mM) was added. The seeds formed in this solution are about 2-3 nm in size. The growth solution is made from a $HAuCl_4$ (0.028 mM, 30 mL) solution containing SOPG (0.0209 g) with NBD-PG (1 Mg). The growth solution was stirred for 20 min at RT. Then 9 mL growth solution was transferred to a vial sitting in an ice bath. $AgNO_3$ (0.05 mL, 1.67 mM), Ascorbic acid (0.05 mL, 9.38 mM) and fresh seed solution (0.2 mL) was added the mixture was inverted for 10 times. The mixture was then put in ice bath for 1 h and then stored in the fridge (4 °C) overnight. This process reproducibly produced 100-200 nm NBD labelled SOPG coated gold nanocubes.

2.7.2 Characterization of NBD labeled SOPG coated gold nanocubes

The absorption spectrum of 100-300 nm NBD labeled SOPG coated gold nanocube was measured in water by Agilent 8453 UV-Vis spectrophotometer. Figure 2.17 shows the UV-vis spectrum of gold nanocubes with an absorption band 471 nm, which corresponds to the absorption of the NBD dye. The surface

plasmon resonance of gold nanocubes is probably masked by the absorption of NBD dye because of the low concentration of gold nanocube.

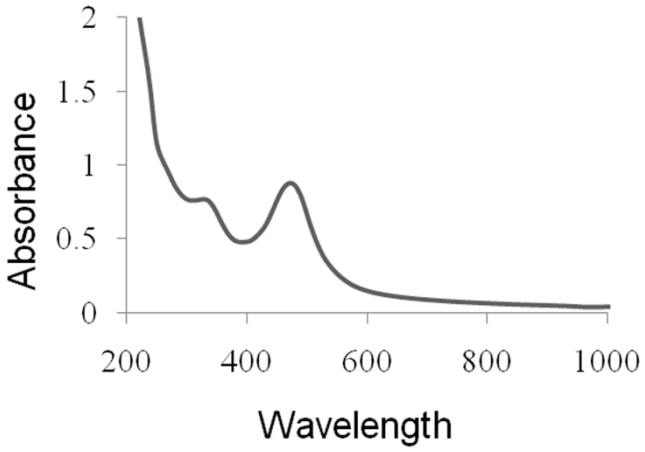

Figure 2.17. The UV-Vis absorption spectrum of 100-300 nm NBD labeled SOPG coated gold nanocubes shows an absorption band at 471 nm.

The size of synthesized NBD labeled SOPG coated gold nanocubes were measured in water by Malvern Nano-S Dynamic Light Scattering. The dynamic light scattering provides an estimate of the size distribution by intensity as shown in Figure 2.18. The size distribution shows one peak at 216 nm with a distribution width of 103 nm.

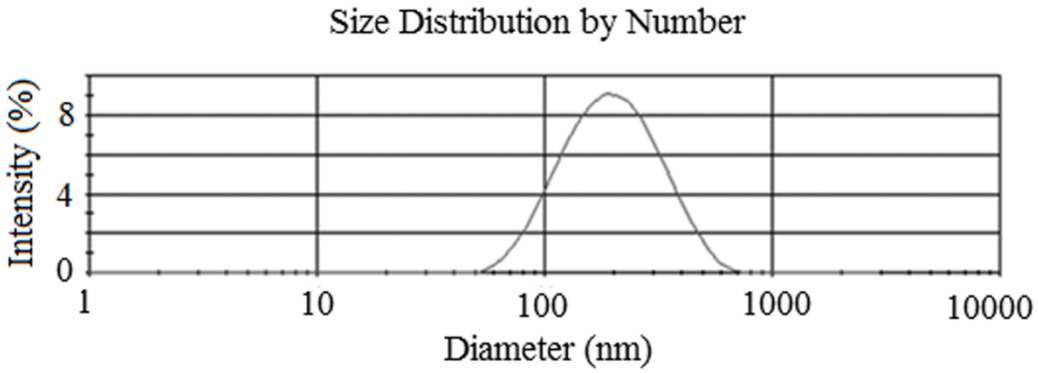

Figure 2.18. Size distribution of NBD labeled SOPG coated gold nanocube in water from dynamic light scatting.

The SEM image of NBD labeled SOPG coated gold nanocubes were taken by Scanning Electron Microscope - Field emission S-4800. As showed in figure 2.19, most of the gold nanocubes show ordered crystal structures of cube. These images also show that the nanocubes are quite uniform in size and have an average diameter of about 200 nm, which is consistent with the DLS distribution.

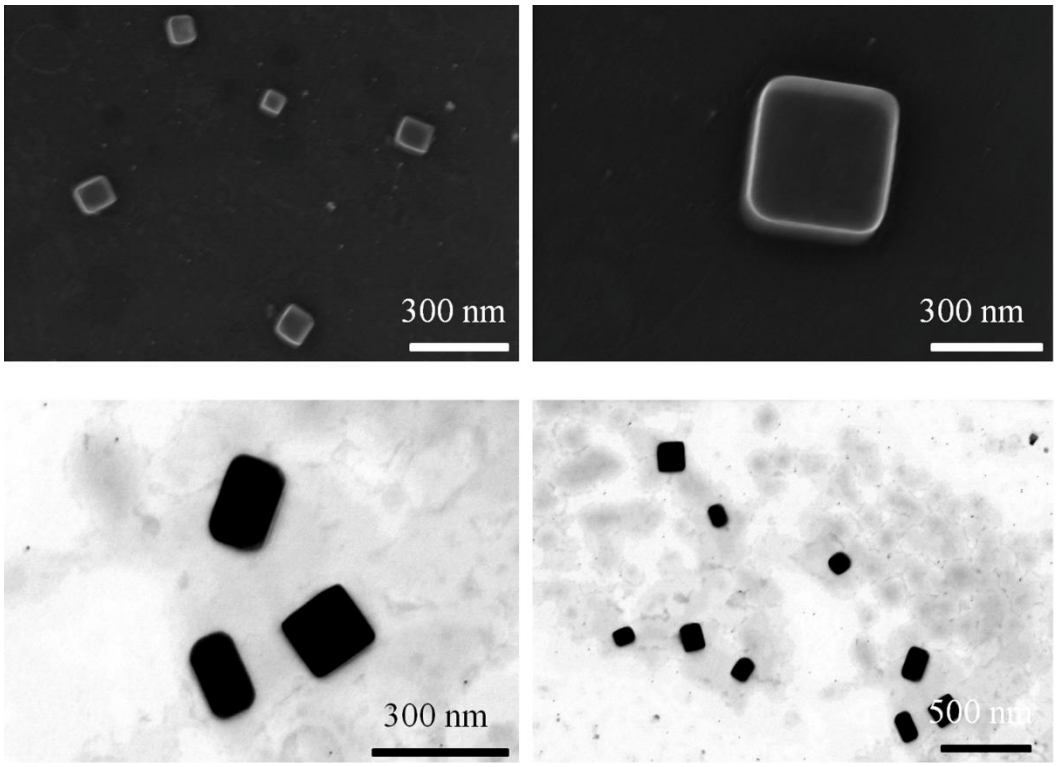

Figure 2.19. The SEM images of 100-200 nm NBD labeled SOPG coated gold nanocube.

2.8 Characterization of concentration and size of NBD-SOPG-GNPs by different techniques

2.8.1 Introduction of Fluorescence Correlation Spectroscopy (FCS)

Fluorescence correlation spectroscopy (FCS) is an analysis to study the fluctuation of fluorescence intensity. The fluctuation of fluorescence intensity is

caused by the thermal equilibrium or Brownian motion of particles. That means the number of particles in the defined focal volume is not consistent and fluctuates randomly around the average number of particles. The analysis of FCS can provide the average number of particles at the focal volume and the average diffusion time when particles passing through the focal volume. Then both size and concentration of particles will be determined.

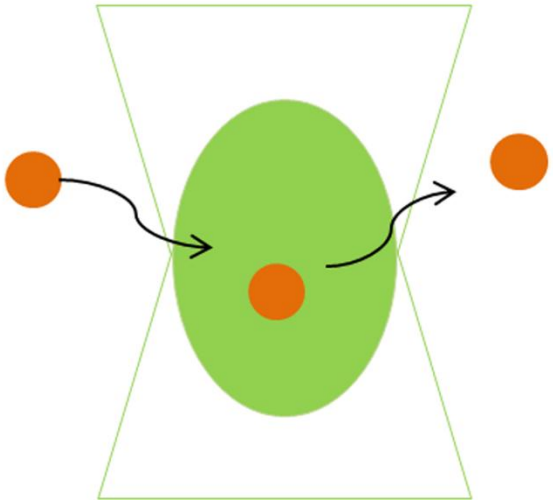

Figure 2.20. Fluorescence correlation spectroscopy measures the fluctuation of fluorescence intensity of particles when they pass through a small focal volume. [Adapted from reference 42]

Theory of FCS

A temporally autocorrelation analysis is performed if only one particular fluorescence signal is focused. In this process, the fluorescence intensity is recorded. The relative fluctuation of the particle number N is given by:

$$\frac{\sqrt{\langle(\delta N)^2\rangle}}{\langle N\rangle} = \frac{\sqrt{\langle(N-\langle N\rangle)^2\rangle}}{\langle N\rangle} = \frac{1}{\sqrt{\langle N\rangle}}$$

As showed in equation 1, the relative fluctuation decreases when the number of particles grows. Thus, it is important to keep the concentration of the measured particles low. Usually, the focal volume is about femtoliter and the temporal average number of particles should be in the range of 0.1 to 100. This corresponds to concentrations between nanomolar (10^{-9} M) to micromolar (10^{-6} M).

The fluorescence signal emitted by molecule is recorded. The fluctuation of the fluorescence signal is then defined as the deviation from the average fluorescence intensity:

$$\delta F(t) = F(t) - \langle F(t) \rangle$$

If all of the fluctuations of fluoreseare signal are from the differences in the local concentration within the effective volume, then the flucturation can be written as

$$\delta F(t) = k \int_V I_{ex}(\underline{r}) \cdot S(\underline{r}) \cdot \delta \left(\sigma \cdot q \cdot C(\underline{r}, t) \right) \cdot dV$$

This equation describes the measured fluorescence from a molecule in a volume dV within a focused beam. The Iex (r) is the inentisty of the laser that varies with the position.

K: detection efficiency of the machine

Iex(r): Beam intensity which varies with position

S(r): collection efficiency of the machine set up

$\delta \left(\sigma \cdot q \cdot C(\underline{r}, t) \right)$: Dynamic of particles, where σ is the absorption cross section of molecule, q is the quantum yield, and $C(r, t)$is the concentration at a specific time and position.

The normalized autocorrelation function is described as:

$$G(\tau) = \frac{\langle \delta F(t) \cdot \delta F(t+\tau) \rangle}{\langle F(t) \rangle^2}$$

This autocorrelation function analyzes the signal of its self-similarity with a lag time τ. The amplitude G(0) is then the variance of the fluctuation of fluorescence intensity δF(t). The autocorrelation function for a free diffusing particle is:

$$\mathrm{G}(\tau) = \frac{1}{\mathrm{V_{eff}}\langle \mathrm{C} \rangle} \cdot \frac{1}{\left(1 + \frac{\tau}{\tau_\mathrm{D}}\right)} \cdot \frac{1}{\sqrt{1 + \left(\frac{\mathrm{r_0}}{\mathrm{z_0}}\right)^2 \cdot \frac{\tau}{\tau_\mathrm{D}}}}$$

Where V_{eff} is the effective focal volume.

Therefore, by knowing the dimensions r_0 and z_0 from calibration measurements, the local concentration of fluorescent molecules can be determined exactly from the amplitude G(0) of the autocorrelation curve:

$$\mathrm{G}(0) = \frac{1}{\langle \mathrm{N} \rangle} = \frac{1}{\mathrm{V_{eff}} \cdot \langle \mathrm{C} \rangle}$$

$$\langle \mathrm{C} \rangle = \frac{1}{\mathrm{V_{eff}} \cdot \mathrm{G}(0)}$$

As we know, the lateral diffusion time τ_D is related to the diffusion coefficient, which is the intrinsic property of the molecule.

$$\tau_\mathrm{D} = \frac{\mathrm{r_0^2}}{4 \cdot \mathrm{D}}$$

So the diffusion coefficient D can be easily derived from the diffusion time τ_D. The mean radius of particles will then be obtained by the Stokes-Einstein equation:

$$\mathrm{R} = \frac{\mathrm{k_B T}}{6\pi\eta \mathrm{D}}$$

where k_B is the Boltzmann constant, T is the temperature, and η is the viscosity of solvent. [43, 44]

2.8.2 Determination of size and concentration of 30 nm NBD-SOPG-GNPs

In this experiment, the 30 nm NBD-SOPG-GNPs with different concentration was measured by FCS at 488 nm. The number of particles and diffusion time were measured directly by this experiment. As showed in Figure 2.21, the number of particles changed linearly when the solution of NBD-SOPG-GNPs is diluted. The concentration of NBD-SOPG-GNPs can be easily derived from the number of particles as the focal volume is known. Furthermore, the radius r of GNPs can be determined by:

$$N_{\text{gold atoms per particle}} = \frac{C_{Au^{3+}}}{C_{GNPs}}$$

$$V_{GNPs} = V_{\text{gold atom}} \times N_{\text{gold atoms per particle}} = \frac{4}{3}\pi r^3$$

Where $V_{\text{gold atom}} = 16.9\text{Å}^3$.

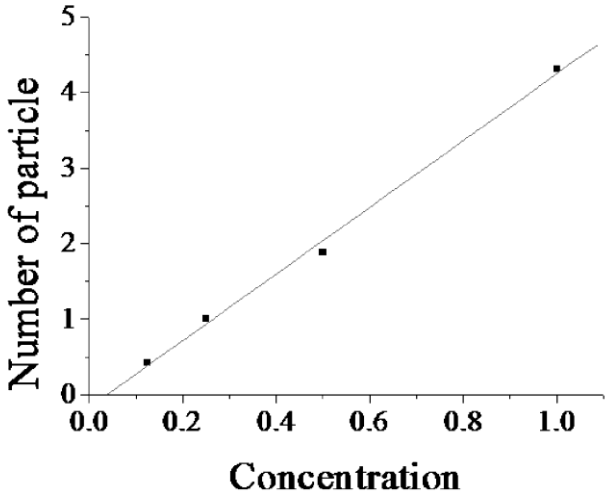

Figure 2.21. The number of particles changed linearly when concentration of NBD-SOPG-GNPs is diluted linearly.

Diffusion coefficient is an important intrinsic character of the particle, which can be obtained by its relationship with the diffusion time τ_D:

$$\tau_D = \frac{\omega_0^2}{4 \cdot D}$$

The diffusion coefficient depends on temperature, viscosity and the size of particles. So we can get the radius of particles based on:

$$D = \frac{kT}{6\pi\eta r}$$

Figure 2.22 shows diffusion time of 30 nm NBD-SOPG-GNPs as the concentration changed. However, the diffusion time is not consistent as the concentration decrease. Here, we get a range of the radius 206 ± 110 nm.

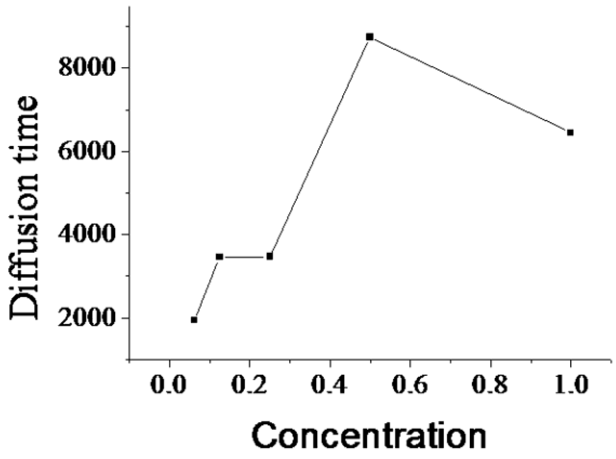

Figure 2.22. The diffusion time of NBD-SOPG-GNPs at different concentration.

We have a summary of size in table 2.3 by combining the informaiton from DLS, SEM and FCS. As shown in table 2.3, DLS, SEM, and the N of FCS gave the similar size of 30 nm. However, the size from diffusion time is bigger.

Table 2.3. The size of GNPs determined by different techniques

	Diameter, nm
DLS	30 ± 9 nm
SEM	30 ± 4 nm
FCS, N	30 ± 1 nm
FCS, τ	206 ± 110 nm

Reference

1. Rad, A. G., Abbasi, H., Afzali, M. H. Gold Nanoparticles: Synthesising, Characterizing and Reviewing Novel Application in Recent Years. *Physics Procedia*, **2007**, 22, 203-208.
2. Pissuwan, D., Niidome, T., Cortie, M. B. The forthcoming applications of gold nanoparticles in drug and gene delivery systems. *Journal of Controlled Release*, **2011**, 149, 65-71.
3. Daniel, M. C., Astruc, D. Gold Nanoparticles: Assembly, Supramolecular Chemistry, Quantum-Size-Related Properties, and Applications toward Biology, Catalysis, and Nanotechnology. *Chemical Reviews*, **2004**, 104, 293-346.
4. Ribeiro, N. F. P., Mendes, F. M. T., Perez, C. A. C. et al. Selective CO oxidation with nano gold particles-based catalysts over Al_2O_3 and ZrO_2 . *Applied Catalysis A: General*, **2008**, 347, 62-71.
5. Schubert, M. M., Hackenberg, S., Veen, A. C. V. et al. CO Oxidation over Supported Gold Catalysts - "Inert" and "Active" Support Materials and Their Role for the Oxygen Supply during Reaction. *Journal of Catalysis*, **2001**, 197, 113-122.
6. Polte, J., Erler, R., Thünemann, A. F. et al. Nucleation and Growth of Gold Nanoparticles Studied via in situ Small Angle X-ray Scattering at Millisecond Time Resolution. *ACS Nano*, **2010**, 4, 1076-1082.

7. Turkevich, J., Stevenson, P. C., Hillier, J. A study of the nucleation and growth processes in the synthesis of colloidal gold. *Discuss. Faraday Soc*., **1951**, 11, 55-75.
8. Frens, G. Controlled Nucleation for the Regulation of the Particle Size in Monodisperse Gold Suspensions. Nature (London), *Phys. Sci*., **1973**, 241, 20-22.
9. Pong, B. K., Elim, H. I., Chong, J. X. et al. New Insights on the Nanoparticle Growth Mechanism in the Citrate Reduction of Gold(III) Salt: Formation of the Au Nanowire Intermediate and Its Nonlinear Optical Properties. J. Phys. Chem. C., 2007, 111, 6281-6287.
10. Brust, M., Schiffrin, D. J., Bethell, D. et al. Novel gold-dithiol nano-networks with non-metallic electronic properties. *Advanced Materials*, **1995**, 7, 795-797.
11. Manna, A., Chen, P. L., Akiyama, H. et al. Optimized Photoisomerization on Gold Nanoparticles Capped by Unsymmetrical Azobenzene Disulfides. *Chem. Mater*., **2003**, 15. 20-28.
12. Martin, M. N., Basham, J. I., Chando, P. et al. Charged Gold Nanoparticles in Non-Polar Solvents: 10-min Synthesis and 2D Self-Assembly. *Langmuir*, **2010**, 26, 7410-7417.
13. Chithrani, B. D., Chan, W. C. Elucidating the mechanism of cellular uptake and removal of protein-coated gold nanoparticles of different sizes and shapes. *Nano Lett*., **2007**, 7, 1542-50.

14. Rosi, N. L., Giljohann, D. A., Thaxton, C. S. et al. Oligonucleotide-modified gold nanoparticles for intracellular gene regulation. *Science*, **2006**, 312, 1027-30.
15. Samad, A., Sultana, Y., Agil, M. Liposomal drug delivery systems: an update review. *Curr Drug Deliv*., **2007**, 4, 297-305.
16. Puri, A., Loomis, K., Smith, B. et al. Lipid-based nanoparticles as pharmaceutical drug carriers: from concepts to clinic. *Crit Rev Ther Drug Carrier Syst*., **2009**, 26. 523-80.
17. Zhu, H., Tao, C., Zheng, S. et al. One step synthesis and phase transition of phospholipid-modified Au particles into toluene. *Colloids and Surfaces A: Physicochemical and Engineering Aspects*, **2005**, 257 - 258, 411-414.
18. Rosi, N. L., Mirkin, C. A. Nanostructures in biodiagnostics. *Chem Rev*., **2005**, 105, 1547-62.
19. Ma, G., Allen, H. C. Condensing effect of palmitic acid on DPPC in mixed Langmuir monolayers. *Langmuir*, **2007**, 23, 589- 97.
20. Bakshi, M. S., Possmayer, F., Petersen, N. O. Role of Different Phospholipids in the Synthesis of Pearl-Necklace-Type Gold−Silver Bimetallic Nanoparticles as Bioconjugate Materials. *J. Phys. Chem. C*., **2007**, 111, 14113-14124.
21. Khlebtsov, N. G., Dykman, L. A. Optical properties and biomedical applications of plasmonic nanoparticles. *Journal of Quantitative Spectroscopy and Radiative Transfer*, **2010**, 111, 1-35.

22. Khlebtsov, B. N., Khlebtsov, N. G. Biosensing potential of silica/gold nanoshells: Sensitivity of plasmon resonance to the local dielectric environment. *Journal of Quantitative Spectroscopy and Radiative Transfer*, **2007**, 106, 154-169.
23. Link, S., EI-Sayed, M. A. Size and Temperature Dependence of the Plasmon Absorption of Colloidal Gold Nanoparticles. *J. Phys. Chem. B.*, **1999**, 103, 4212-4217.
24. Hallett, F. R. Particle size analysis by dynamic light scattering. *Food Research International*, **1994**, 27, 195-198.
25. Horne, D. S. Analytical Methods | Light Scattering Techniques. *Encyclopedia of Dairy Sciences (Second Edition)*, **2011**, 133-140.
26. Nose, T. 2.10 – Light Scattering, *Polymer Science: A Comprehensive Reference*, **2012**, 2, 301-329.
27. Schultz, N., Metreveli, G., Franzreb, M. et al. Zeta potential measurement as a diagnostic tool in enzyme immobilisation. *Colloids Surf B Biointerfaces*, **2008**, 66, 39-44.
28. Biermann, C. J. 21 – Colloid and Surface Chemistry, *Handbook of Pulping and Papermaking (Second Edition)*, **1996**, 421-437.
29. Moore, J., Cerasoli, E. Particle Light Scattering Methods and Applications. *Encyclopedia of Spectroscopy and Spectrometry (Second Edition)*, **2010**, 2077-2088.

30. Mitri, K., Shegokar, R., Gohla, S. et al. Lipid nanocarriers for dermal delivery of lutein: preparation, characterization, stability and performance. *Int J Pharm*, **2011**, 414, 267-75.
31. Greenwood, R., Kendall, K. Selection of Suitable Dispersants for Aqueous Suspensions of Zirconia and Titania Powders using Acoustophoresis, *Journal of the European Ceramic Society*, **1999**, 19, 479-488(10).
32. Hanaor, D., Michelazzi, M., Leonelli, C. et al. The effects of carboxylic acids on the aqueous dispersion and electrophoretic deposition of ZrO_2. *Journal of the European Ceramic Society*, **2012**, 32, 235-244.
33. Müller, S. A., Aebi, U., Engel, A. What transmission electron microscopes can visualize now and in the future. *J Struct Biol*., **2008**, 163, 235-45.
34. Dwyer, C. Chapter Three – Atomic-Resolution Core-Level Spectroscopy in the Scanning Transmission Electron Microscope. *Advances in Imaging and Electron Physics*, **2013**, 175, 145-199.
35. Suvorova, A. A., Samarin, S. Secondary electron imaging of SiC-based structures in secondary electron microscope. *Surface Science*, **2007**, 601, 4428-4432.
36. Fultz, B., Howe, J. Transmission Electron Microscopy and Diffractometry of Materials (Third edition). *Springer*, Heidelberg, **2007**.
37. Romeu, D., Gomez, A., Reyes-Gasga, J. Nanowires - Fundamental Research, Chapter 20 Electron Diffraction and HRTEM Structure Analysis of Nanowires. *InTech*., **2011**.

38. Klechkoyskaya, V. Electron Diffraction Structure Analysis. *Electron Crystallography NATO Science Series II: Mathematics, Physics and Chemistry*, **2006**, 211, 85-96.
39. Stubbs II, M. T. Protein Crystallography. *Comprehensive Medicinal Chemistry II*., **2007**, 3, 449-472.
40. Liz-Marzán, L. M., Giersig, M., Mulvaney, P. Synthesis of Nanosized Gold−Silica Core−Shell Particles. *Langmuir*, **1996**, 12, 4329-4335.
41. Ivanov, M. R., Bednar, H. R., Haes, A. J. Investigations of the Mechanism of Gold Nanoparticle Stability and Surface Functionalization in Capillary Electrophoresis. *ACS Nano*., **2009**, 3, 386-394.
42. Anikovsky, M., Wiltshire, Z. D., Weisshart, K. et al. Photon counting histogram analysis for two-dimensional systems. *Chemphyschem*, **2011**, 12, 2439-48.
43. Chen, H., Farkas, E. R., Webb, W. W. Chapter 1: In vivo applications of fluorescence correlation spectroscopy. *Methods Cell Biol*., **2008**, 89, 3-35.
44. Schwille, P., Haustein, E. Fluorescence Correlation Spectroscopy - An Introduction to its Concepts and Applications. *Spectroscopy*, **2009**, 94, 1-33.

Chapter 3: The uptake of lipid-coated gold nanoparticles to different cell lines

3.1 Introduction

Metal nanoparticles, especially gold, are particularly promising because they on the one hand are inert but on the other hand can be derivatized on the surface to provide high and specific binding capacity. [1, 2] Furthermore, the optical properties of GNPs make them interesting tools in the cancer diagnostics and photo thermal therapeutics. [3] The wide-spread use of GNPs is also helped by the ease of preparation and control of size.

In order to design GNP-based drug delivery and therapy systems, we need a thorough understanding of the uptake mechanism of GNPs in cells. [4] It has been suggested that the shape and size of GNPs play important roles in the cellular uptake process. [5] In fact, a recent study of the uptake kinetics and mechanism of GNPs showed that spherical GNPs with a diameter of around 20-50 nm were most readily taken up by cells in culture. [6]

One possible route of exposure to GNPs is through inhalation, which in turn means that the lung epithelial cells will be the first to come in contact with the GNPs. The most important function of the type II alveolar epithelial cell (type II pneumocyte) is the secretion of lung surfactants. [7] Lung surfactants are important for the function of the alveolar system and work by forming a monolayer at the interface between the liquid around the cells and air in the alveolar spaces. This reduces the surface tension of the alveolar epithelium and allows for easy breathing. [8] The type II alveolar epithelial cells contain well-characterized organelles called lamellar bodies (LBs), which have tightly packed, multiple membrane liposomes surrounded by a limiting membrane. [9] After

synthesis, lung surfactant is packed into the LBs and delivered to the plasma membrane for exocytosis into the alveolar fluid where they form tubular myelin that in turn forms the surfactant monolayer structure. A considerable portion of the secreted surfactants (25%-95%) will be recycled by an endocytic pathway such as clathrin coated pits forming clathrin coated vesicles (CCVs), which suggests that these cells will readily take up lipid coated particles. [10] The A549 human lung adenocarcinoma cell line has been established as a good *in vitro* model for the type II epithelial cells of the lung. [11] We speculate that the phospholipid coated GNPs may be endocytosed and excreted by A549 cells by using pathways designed for the lung surfactant. Accordingly, we chose to investigate the uptake and fate of 30 nm GNPs coated with 1-stearoyl-2-oleoyl-*sn*-glycero-3-phospho-(1'-*rac*-glycerol) (SOPG) in A549 cells. In order to use fluorescence as a means of tracking the GNPs in live cells, we introduced a small amount of 7-nitro-2-1,3-benzoxadiazol-4-yl (NBD) labeled SOPG (NBD-PG) into the SOPG bilayer.

3.2 Experiment section

A549 cells were grown in F-12K medium with 10% fetal bovine serum (FBS) at 37 ^{0}C with 5% CO_2. C2C12 cells were grown in DMEM medium with 10% FBS at 37 ^{0}C with 5% CO_2. The C2bbe1 cells were grown in DMEM medium with 10% FBS and 0.003% transferrin at 37 °C with 5% CO_2.

3.2.1 Materials

The A549 cell lines (ATCC® CCL-185™), C2C12 cells (ATCC® CRL-1772™) and C2bbe1 cells (ATCC® CRL-2102™) were purchased from American Type

Culture Collection (ATCC,). F-12K medium, DMEM medium, fetal bovine serum (FBS), and 0.25% Trypsin-EDTA and dyes 4′, 6-diamidino-2-phenylindole (DAPI), LysoTracker Red (DND 99), MitoTracker Red, rabbit anti PMP 70 antibody, Cy3 goat anti-rabbit antibody, CellLight® Lysosomes-RFP, BacMam 2.0 were obtained from Invitrogen. Anti-LAMP1 antibody [1D4B] - BSA and Azide free (ab25245) was obtained from abcam, Anti-rat IgG (H+L), (Alexa Fluor® 555 Conjugate) #4417 was bought from Cell Signaling Technology, Inc.

3.2.2 Flow Cytometry

Cells grown in proper medium at 37 °C were incubated with NBD-SOPG-GNPs for the 24 hrs at the concentration of 0.06 nM. The cells were detached from the culture dish with 0.25% trypsin and the suspension was centrifuged at 1100 rpm (g = 250) for 4 min to remove the supernatant. Cells were then fixed by 1% paraformaldehyde (PF) for 30 min, centrifuged again and resuspended in Phosphate buffered saline buffer (PBS). The cells were removed from the culture dishes and the fluorescence intensity per cell was measured in a flow cytometer (Fluorescence Activated Cell Sorter – FACS). Flow cytometry analysis was performed using a FACS Calibur and the BD CellQuest Pro software (Becton Dickinson, Franklin Lakes, NJ). All results are given relative to a control sample containing untreated cells.

3.2.3 Confocal imaging

Cells were grown in 35 mm uncoated glass bottom dishes (glass thickness: No. 1.0, diameter: 14 mm). After they reached 60% confluence, the cells were incubated with 1 mL medium with NBD-SOPG-GNPs (0.06 nM) for different

times. After the incubation, the cells were fixed with 4% PF for 0.5 hours at RT. To study co-localization with acidic compartments, cells were stained with fresh LysoTracker Red solution (DND 99, 3.4 μM) for 45 min, and then fixed with 4% PF for 0.5 hrs. To study co-localization with lysosome, cells were cultured with mixture of lysosome-RFP^{TM} (30 μL) and 1 mL medium for 24 hrs. To study co-localization with mitochondria, cells were stained with MitoTracker Red (0.46 μM) for 15 min, then fixed with 4% PF for 0.5 hrs. To study co-localization with peroxisomes, cells were fixed with 4% PF for 15 min and permeabilized with 0.2% triton X-100 for 5 min, followed by immunolabelling with the primary antibody anti peroxisomal membrane protein 70 (anti-pmp70) for 2 hrs and with the secondary antibody (Cy3 Goat Anti-Rabbit IgG (H+L)) for 30 min. Nuclei were stained with 4′, 6-diamidino-2-phenylindole (DAPI). Cells were imaged with an LSM500 confocal microscope (Zeiss) using lasers at 364 nm, 488 nm 561 nm and 594 nm depending on the dye used.

3.2.4 The uptake process of NBD-SOPG-GNPs studied by electron microscope

The cells were grown in proper medium at 37 °C with 5% CO_2 and incubated with NBD-SOPG-GNPs (0.06 nM) for the times indicated in the experiments. After washing three times with PBS, the cells were fixed with 2.5% glutaraldehyde and 2% paraformaldehyde/cacodylate buffer for 1 hr at RT. After fixation, cells were washed twice with 0.1 M cacodylate buffer and kept in the cacodylate buffer overnight at 4 °C. The cells were rinsed with 0.1 M cacodylate buffer 2x10 min; fixed with 1% OsO_4 in cacodylate buffer for 100 min at RT; and rinsed with water three times. The cells were then dehydrated by a graded ethanol solution process

(50% alcohol, 10 min; 70% alcohol, 10 min; 70% alcohol + 1% uranyl acetate, 2.5 hrs at RT and overnight at 4 °C; 90% alcohol, 10 min; 100% alcohol, 10 min×3). The cells were infiltrated with a series of embedding resins (Spurr's resin:100% alcohol, 1:3, 2 hrs; Spurr's resin:100% alcohol, 1:1, 2 hrs; Spurr's resin:100% alcohol, 3:1, 2 hrs; Spurr's resin, overnight with lid open; Spurr's resin, 3 hrs ×2). Then cells were embedding at 65 °C oven overnight with Spurr's resin. Ultrathin (70-100 nm) sections of cells were cut with a diamond knife. Cut cells were then loaded onto carbon-coated TEM grids. The TEM images of cells were obtained with a Scanning Electron Microscope - Field emission S-4800 in the TEM mode. [12, 13]

3.2.5 The exocytosis process of NBD-SOPG-GNPs studied by electron microscope

In these experiments, cells were exposed to NBD-SOPG-GNPs (0.06 nM) for 24 hrs. Then cells were washed with PBS three times to remove the GNPs. Then cells were allowed to grow for another 24 hrs, 48 hrs, 72 hrs, or 96 hrs. After the allotted time, cells were fixed and prepared for the TEM experiments.

3.2.6 Image cross correlation spectroscopy (ICCS)

Image correlation spectroscopy (ICS) is a spatial fluctuation analysis technique which correlates the fluctuations in fluorescence intensity across an image to obtain information about the number of fluorescent particles per unit area. [14, 15] The amplitude of the autocorrelation function of a single image can be shown to be inversely proportional to the average number of fluorescent particles per beam area. Since the beam area is known, the cluster density (CD) can be calculated as

the number of clusters (particles, molecules, compartments) per square micrometer.

$$CD = \frac{\langle n_p \rangle}{\pi \omega_0^2} = \frac{1}{g(0,0)\pi\omega_0^2} \quad (1)$$

Image cross correlation spectroscopy (ICCS) uses the cross correlation function calculated from two images collected from the same area of a cell to obtain information about the number of clusters which contain two separate species, imaged individually in the pair of images. Usually, two different fluorophores, such as green and red, are used to label the particles of interest. The two colors, red and green, were collected by confocal microscopy at high magnification to ensure oversampling. This yields two images, one representing the distribution of NBD-SOPG-GNPs (green) and the other is acidic compartments labeled with LysoTracker red (red). Then the time independent, spatial cross correlation of the two images is given by:

$$r_{gr}(\xi, \eta) = \frac{\langle \delta i_g(x,y) \delta i_r(x+\xi, y+\eta) \rangle}{\langle i_g(x,y) \rangle \langle i_r(x,y) \rangle} \quad (2)$$

The cross correlation function is fitted to a 2D Gaussian to extract the amplitude ($g_{gr}(0,0)$), the beam width (ω_o), and the offset at infinite distance ($g_{gr\infty}$)

$$r_{gr}(\xi, \eta) = g_{gr}(0,0) \exp\left[-\frac{\xi^2 + \eta^2}{\omega_0^2}\right] + g_{gr\,\infty} \quad (3)$$

The amplitude, $g_{gr}(0,0)$, is an estimate of the number of particles which contain both green and red species within the beam area relative to the number of particles that contain green species and the number of particles that contain red species. From this we calculate the CD of green and red particles by:

$$CD_{gr} = \frac{g_{gr}(0,0)}{g_g(0,0) g_r(0,0) \pi \omega_{gr}^2} \quad (4)$$

Here $g_g(0,0)$ and $g_r(0,0)$ represent the average total number of particles of the green and red species respectively. As a consequence, the fraction of green that is co-localized with the red and the fraction of red co-localized with green can be calculated by:

$$F(g/r) = \frac{CD_{gr}}{CD_g} = \frac{g_{gr}(0,0)}{g_r(0,0)} \quad (5)$$

$$F(r/g) = \frac{CD_{gr}}{CD_r} = \frac{g_{gr}(0,0)}{g_g(0,0)} \quad (6)$$

3.2.7 Cell number measured by Coulter counter.

In these experiments, cells were grown for a total of 72 hrs (about 2 cell cycles) without exposure to NBD-SOPG-GNPs (control) or with exposure to NBD-SOPG-GNPs (0.06 nM) for the first 24 hrs, for the first 48 hrs, and for the entire 72 hrs. Later, all of the cells were detached and suspended in the PBS buffer in preparation for Coulter counter. In the counting process, the cell number was measured by mixing 100 μL cell suspensions with 10 mL Isoton II solution. The Coulter Counter takes 0.5 mL mixture to count at each time.

3.3 NBD-SOPG-GNPs were readily internalized by A549 cells

Figure 3.1 shows the histogram of fluorescence distribution of untreated A549 cells (black) or A549 cells treated with NBD-SOPG-GNPs (red). The mean fluorescence increased almost 1000 times after the 24 hr exposure to NBD-SOPG-GNPs. Similarly treated cells were studied by confocal microscopy and the fluorescence image (Figure 3.2) shows that the NBD-SOPG-GNPs (green) are located inside the cell and that none of them are associated with the plasma membrane (stained red with a lipophilic dye (2Z)-2-[(E)-3-(3,3-dimethyl-1-

octadecylindol-1-ium-2-yl)prop-2-enylidene]-3,3-dimethyl-1-octadecylindole, perchlorate, DiI). Equally important, none of the NBD-PG is transferred from the bilayer around the GNPs to any of the cellular membrane structures. There appears to be no fusion with or leakage to other membranes.

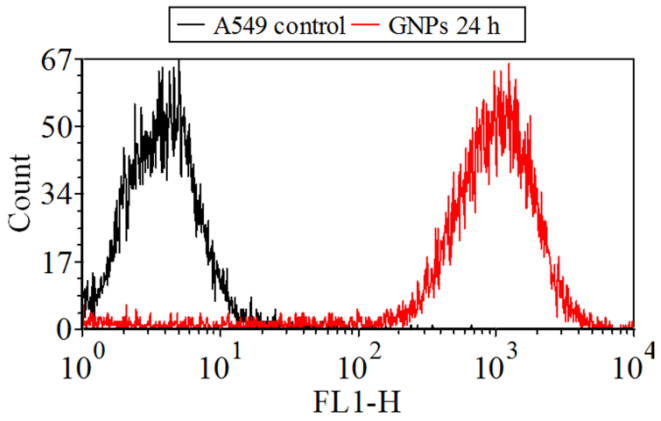

Figure 3.1. The interaction of NBD-SOPG-GNPs with A549 cells. Histogram of the number of A549 cells with a particular fluorescence count for untreated cells (black) and cells treated with NBD-SOPG-GNPs (red). The histogram shows that the mean fluorescence increased nearly 1000 times after 24 hrs treatment.

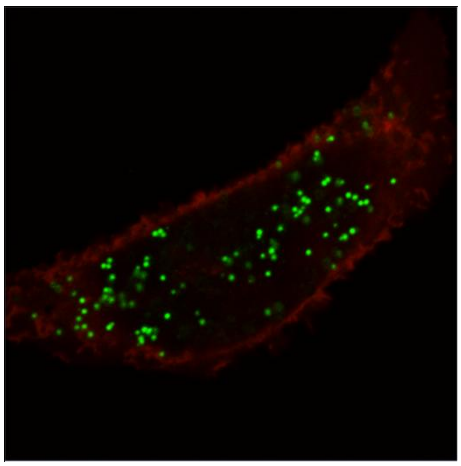

Figure 3.2. Confocal image of NBD-SOPG-GNPs (green) showing that the nanoparticles were readily taken up by the A549 cells and at 24 hrs none of them were associated with the surrounding of cell membrane (stained by DiI in red).

3.4 The NBD-SOPG-GNPs localize to acidic compartments and lysosomes

In order to identify where NBD-SOPG-GNPs are located in the A549 cells, we stained different compartments of the cell by specific dyes.

The three images in Figure 3.3 (A) shows the nucleus in each cell as labeled with DAPI staining (Figure 3.2 A1, blue color) and it is evident from the merged images (Figure 3.2 A3) that none of the NBD-SOPG-GNPs (Figure 3.3 A2, green color) enter the nucleus. The three images in Figure 3.3 (B) shows the lack of co-localization of the green NBD-SOPG-GNPs with mitochondria stained with MitoTracker Red (Figure 3.3 B1, red colour). This is in contrast to a previous report that showed CTAB coated gold nanorods selectively accumulated in or at the edges of mitochondria in A549 cells, causing mitochondrial damage and subsequent cell death. [16] We see no evidence of corresponding co-localization or cell death, suggesting that the membrane coating is less toxic to the A549 cells

than the CTAB coating. The three images in Figure 3.3 (C) compare the intracellular distribution of NBD-SOPG-GNPs and peroxisomes, which are labeled with the peroxisome kit (Figure 3.3 C1, red color), and demonstrate clearly that there is no co-localization. [17]

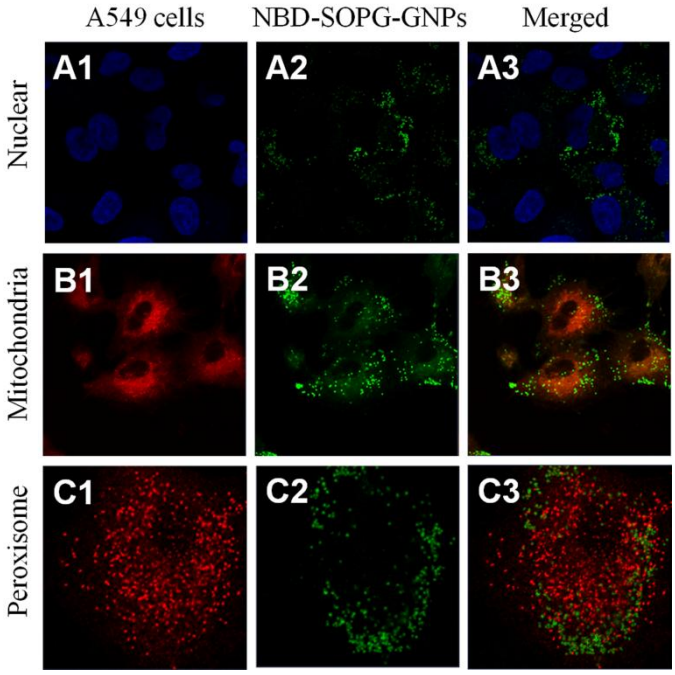

Figure 3.3. Comparison of the localization of NBD-SOPG-GNPs incubated for 72 hrs with various intracellular organelles in A549 cells. The first column of images shows the distribution of the indicated organelles (blue or red), the second column of images shows the distribution of NBD-SOPG-GNPs (green), and the third column contains the merged images. The NBD-SOPG-GNPs accumulate around the peri-nuclear area, but do not penetrate into the nucleus (A). Likewise, the NBD-SOPG-GNPs do not associate with the mitochondria (B) or peroxisomes (C).

Finally, the three images in Figure 3.4 (A) shows a significant co-localization of the green NBD-SOPG-GNPs with the acidic compartments labeled in red with

LysoTracker Red (DND 9) (Figure 3.4 A1, red color). To further confirm if the acidic compartments are lysosomes, we did the co-localization with lysosomes (Figure 3.4 B1, red color). The merged image in Figure 3.4 B3 shows a significant co-localization of the green NBD-SOPG-GNPs with the lysosomes.

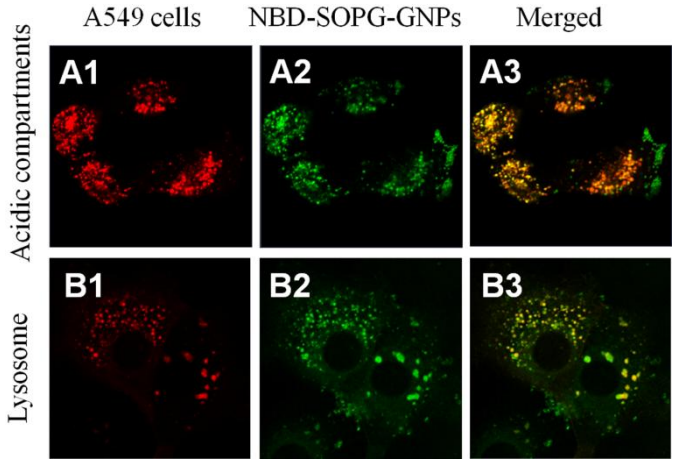

Figure 3.4. The green NBD-SOPG-GNPs are qualitatively highly co-localized with the acidic compartments labeled with LysoTracker Red (A). (B) Shows a significant co-localization of the green NBD-SOPG-GNPs with lysosomes which are labeled by Lysosome-RFP^{TM}.

3.5 NBD-SOPG-GNPs co-localize exclusively in acidic compartments and are then cleared

Figure 3.5 illustrates qualitatively that the extent of co-localization of the NBD-SOPG-GNPs to the acidic compartments increases with time of incubation between 24 hrs and 120 hrs. The extent of co-localization of the two fluorescent components can be quantified using ICCS. [14, 15] This image analysis approach provides a quantitative estimate of the average number of clusters of the acidic compartments from the autocorrelation of a series of red images; a quantitative

estimate of the average number of clusters of the NBD-SOPG-GNPs from the autocorrelation of a series of green images; and a quantitative estimate of the average number of clusters that contain both the acidic compartments and the NBD-SOPG-GNPs from the cross-correlation of a series of pairs of red and green images (See methods for detail).

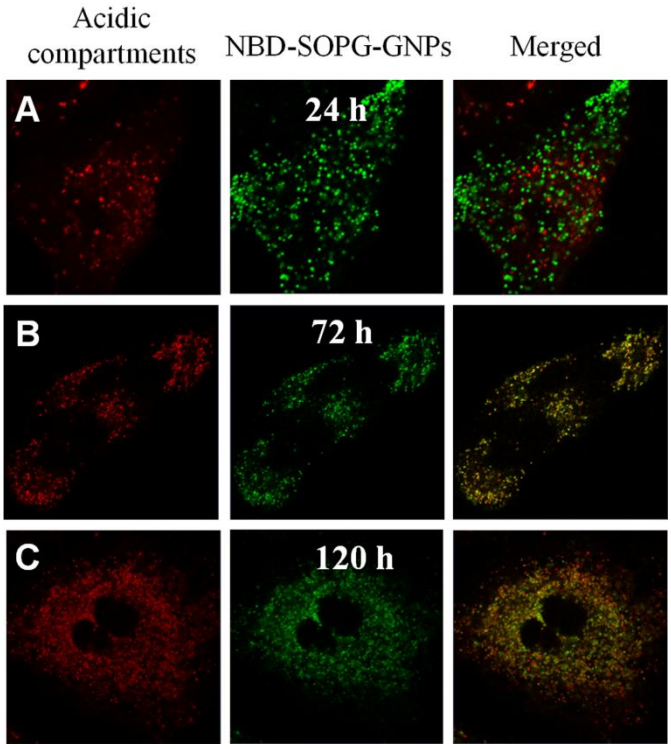

Figure 3.5. Comparison of the localization of acidic compartments of the A549 cell (first column of images in red) with the localization of NBD-SOPG-GNPs (second column of images in green) through the merged images (third column of images) following incubation for 24 hrs (A-row), 72 hrs (B-row), and 120 hrs (C-row).

The results of the autocorrelation analyses are shown in Table 3.1. The cluster density of red particles (CDr) illustrates that the average number of acidic

compartments per square micrometer in the A549 cells remains relatively constant throughout the period of incubation at a value of about three acidic compartments per square micrometer. The cluster density of green particles (CDg) shows that the density of clusters of NBD-SOPG-GNPs reaches a plateau of about three clusters per square micrometer before 24 hrs and that this decreases by close to a factor of two at 120 hrs of incubation. This suggests that the GNPs may be cleared from the cells after extended periods of exposure.

The results of the cross-correlation analyses are also shown in Table 3.1. The value of F(g/r) is an estimate of the fraction of the NBD-SOPG-GNPs that are co-located with the acidic compartments. As a function of the incubation time, this fraction rises from about 0.47 to 0.97 between 24 hrs and 120 hrs suggesting that with time all of the GNPs accumulate in the acidic compartments. Conversely, the parameter F(r/g) shows the fraction of acidic compartments that contain NBD-SOPG-GNPs. As a function of incubation time, this rises from 0.57 at 24 hrs, to a maximum of 0.90 at 72 hrs and then decreases significantly to about 0.68 after 120 hrs. This suggests that over time almost all of the acidic compartments accumulate GNPs within them, but at longer times, a significant fraction lose their cargo – perhaps as a consequence of these compartments being emptied by normal exocytosis processes that expel their lipid content. The co-localization data support the conclusion that when the NBD-SOPG-GNPs are taken up by A549 cells, they locate exclusively to the acidic compartments, from which they can be exported.

Table 3.1. The autocorrelation analysis of the cluster density of acidic compartments (CDr) and NBD-SOPG-GNPs (CDg). The cross correlation analysis of fraction of the NBD-SOPG-GNPs that are co-located with the acidic compartments F(g/r) and fraction of acidic compartments that are co-located with the NBD-SOPG-GNPs F(r/g). Errors represents the standard error of the mean (SEM) at 95% confidence level.

	24 h	**72 h**	**120 h**
CDr	2.81 ± 0.50	3.12 ± 0.54	2.47 ± 0.61
CDg	3.10 ± 0.79	3.16 ± 0.58	**1.62 ± 0.35**
F(g/r)	0.47 ± 0.08	0.93 ± 0.04	**0.97 ± 0.07**
F(r/g)	0.57 ± 0.14	0.90 ± 0.03	0.68 ± 0.06

The observation that the fraction of acidic compartments containing GNPs decreases with prolonged incubation (Table 3.1, compare F(r/g) values at 72 hrs and 120 hrs, $p<0.001$) is consistent with the observation that the density of NBD-SOPG-GNPs decreases (Table 3.1, compare CDg values at 72 hrs and 120 hrs, $p<0.001$) and both observations are consistent with the GNPs being cleared from the cells with time.

3.6 Exposure to NBD-SOPG-GNPs induces formation of LBs in A549 cells.

The fluorescence and electron microscopy data suggest that the NBD-SOPG-GNPs are internalized in A549 cells and then exclusively co-locate to acidic compartments with morphologies similar to LBs. [18] However, A549 cells are known to contain relatively few LBs unless they are induced by some drugs, such

as cationic amphiphilic structures. [19, 20] Figure 3.6 compares the differential interference contrast (DIC) microscopy images and confocal microscopy images of A549 cells prior to and after exposure to GNPs. It is evident from the DIC images (first column of images) that the cytoplasm in cells exposed to GNPs (B-row) contains a much larger number of bright, vesicular structures than does the cytoplasm in control cells (A-row). These bright, vesicular structures contain the NBD-SOPG-GNPs as can be seen in the three images in the row labeled B. This is even clearer in the three enlarged images in the row labeled C where there is complete overlap of the green fluorescence with the bright vesicles.

These images suggest that the vesicles are formed in response to the exposure to the NBD-SOPG-GNPs, perhaps as a mechanism to absorb and sequester them. Since forward scattering in the FACS is sensitive to cell size and the side (90°) scattering is sensitive to the granularity within cells, the increase in the number of vesicles should be observable in the side scattering measurement of the FACS experiments. Figure 3.7 shows the histogram of the number of cells with a particular level of side scattering for samples of control cells and of samples of cells exposed to GNPs for 24 hrs. The shift in the histogram to higher side scattering levels for the cells exposed to GNPs is consistent with an increase in the number of vesicles. The slight decrease in the forward scattering confirms that the increase in side scattering is caused by increased granularity in the cells rather than increased cell size.

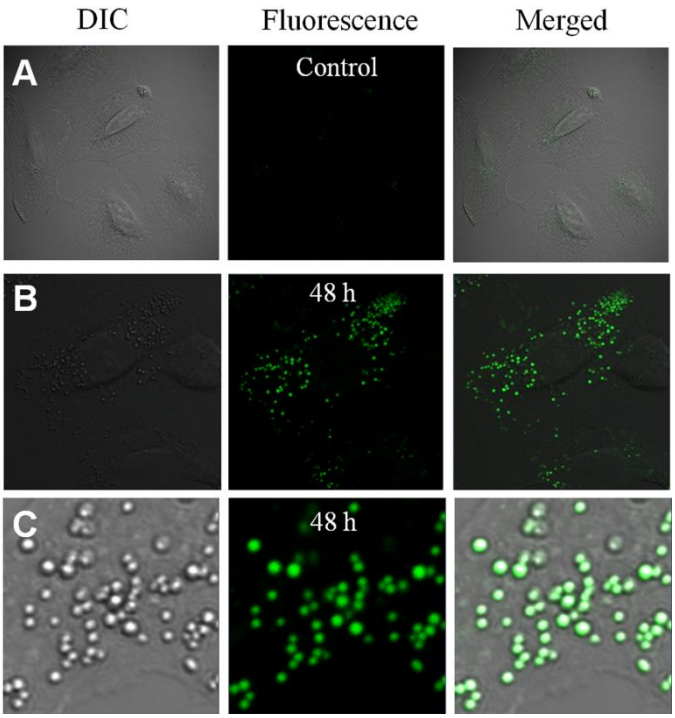

Figure 3.6. The DIC and confocal images of A549 control sample (A) and A549 cells treated with NBD-SOPG-GNPs for 48 hrs (B). (C) High magnification images of A549 cells treated with NBD-SOPG-GNPs for 48 hrs. It is clear that the NBD-SOPG-GNPs co-localize with the granular spots observed inside of A549 cells by DIC.

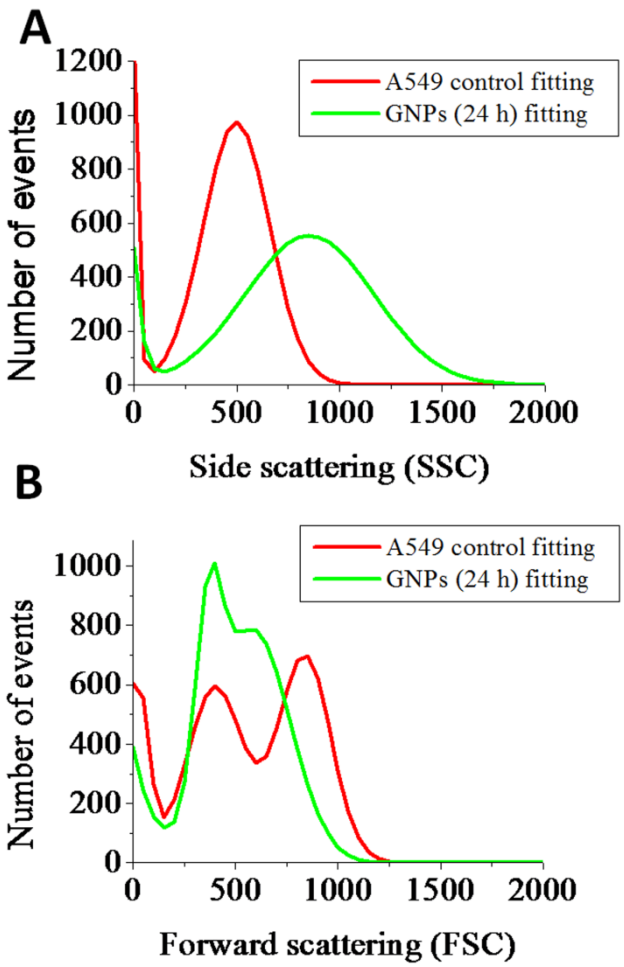

Figure 3.7. (A) Scattering at 90° of A549 cells in control sample (solid line) and of A549 cells after 24 hrs treatment with NBD-SOPG-GNPs (dash line). (B) Forward scattering of A549 cells in control sample (solid line) and of A549 cells after 24 hrs treatment with NBD-SOPG-GNPs (dash line).

3.7 Electron microscope

3.7.1 The uptake process of NBD-SOPG-GNPs studied by electron microscope

These observations of increased numbers of vesicular structures are further confirmed by EM experiments as illustrated in Figure 3.8. As seen in Panel A, there are relatively few vesicular structures in A549 cells that have not been

exposed to GNPs. Similarly, there are only a few such structures in A549 cells that have been exposed for short periods of time (3-6 hrs as seen in panels B and C). In contrast, there are a number of such vesicles in A549 cells exposed to NBD-SOGP-GNPs for longer times as seen in panels D, E and F. Moreover, the vesicles that contain the GNPs are for the most part either multivesicular bodies (MVBs) (24 hrs) or LBs (48 and 72 hrs).

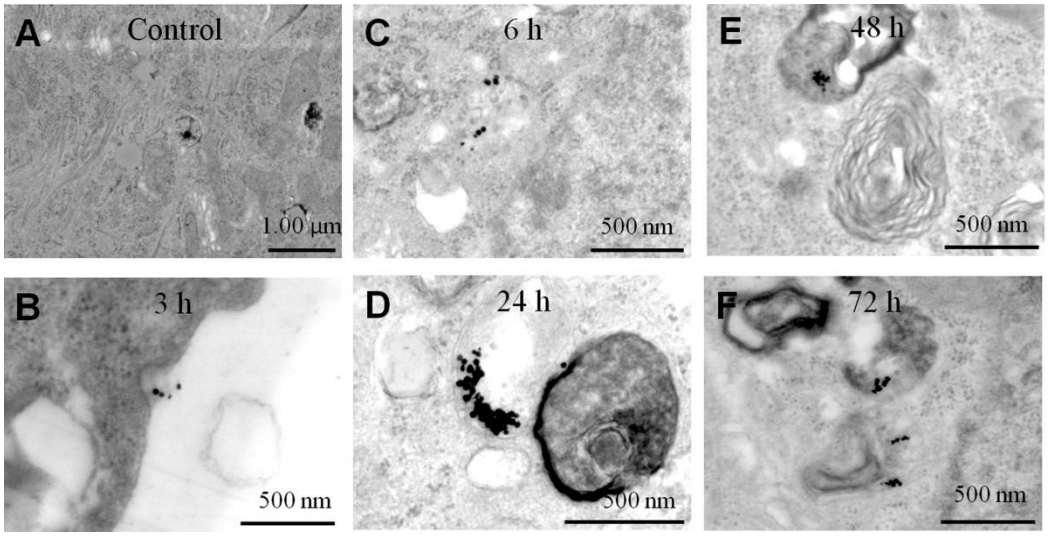

Figure 3.8. Cellular uptake of the 30 nm NBD-SOPG-GNPs into A549 cells in different times. (A) Representative image from the control sample. (B) Image obtained after 3 hrs of exposure to NBD-SOPG-GNPs. (C) Image obtained after 6 hrs of exposure to NBD-SOPG-GNPs where they appear in MVBs in A549 cells. (D) Image obtained after 24 hrs of exposure; most of the GNPs appear in the MVBs and LBs, but a few may be in the cytosol. (E) Image obtained after 48 hrs of exposure; MVBs and LBs are still the main destinations to NBD-SOPG-GNPs. Within the vesicles, the NBD-SOPG-GNPs are relatively dispersed. (F) Image

obtained after 72 hrs of exposure; almost all of the NBD-SOPG-GNPs are in the LBs, with only a few of them in the MVBs.

It is interesting to note that the EM image at 3 hrs may have captured the internalization process in progress. The four nanoparticles appear to incorporate into an invaginated structure with a clearly stained edge, similar to that observed in EM images of coated pits. This would be consistent with the coated pits being the site of internalization of lipids during the recycling of lung surfactant structures.

3.7.2 The exocytosis process of NBD-SOPG-GNPs studied by electron microscope

As shown in Figure 3.9 (B), the GNPs (black dots, arrows) are contained within vesicular structures consistent with morphology similar to that of endocytic vesicles. There were a significant number of these vesicles in each cell (5-40 per cell in a section after 24 hrs). Following 48 hrs, 72 hrs, and 96 hrs of incubation, the NBD-SOPG-GNPs are found in vesicular structures that are morphologically similar to MVBs and LBs. (Figure 3.9 C, D, E, F). [21-24] Qualitatively, it appears that there are fewer vesicles with GNPs as the time proceeds. After 96 hrs, we found only 1 vesicle per 10-20 cells with GNPs (Figure 3.9 (F)). This is qualitatively consistent with the suggestion that some of the lipid coated GNPs are excreted by A549 cells after 72 hrs. Quantitative comparison between the fluorescence and electron microscopy density of vesicles is hampered by the fact that the electron micrographs are obtained from only a thin section (<100 nm) of the cell, which is several micrometers thick. In contrast, the fluorescence

measures signals from all parts of the entire cell. We believe the latter is more reliable as a quantitative assessment of densities of vesicles or clusters of GNPs (Table 3.1).

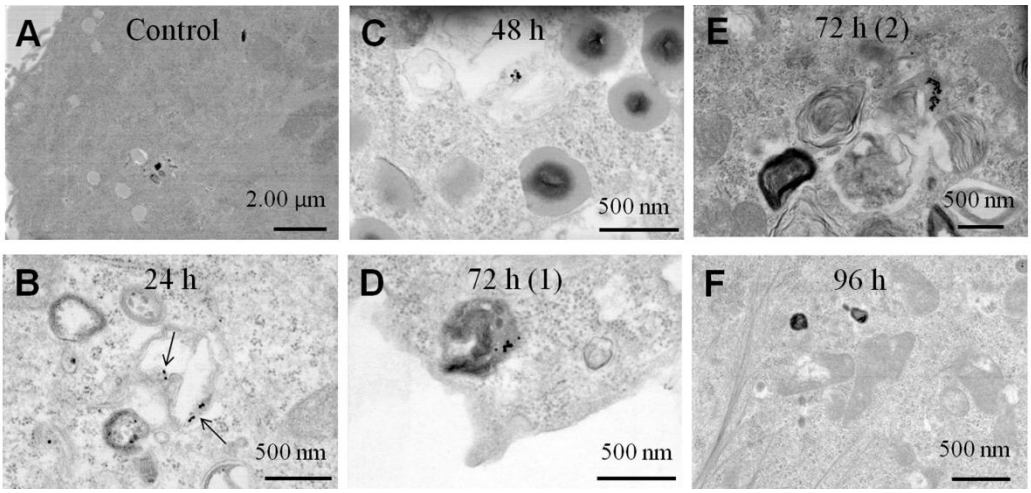

Figure 3.9. Exocytosis of NBD-SOPG-GNPs in A549 cells depends on time. (A) Control sample without NBD-SOPG-GNPs. (B) After 24 hrs of incubation and growth a lot of NBD-SOPG-GNPs were found in MVBs and LBs. (C) After 24 hrs of incubation and 48 hrs of growth NBD-SOPG-GNPs were still found in the MVBs and LBs, but fewer particles were observed than after 24 hrs. (D) After 72 hrs of growth, NBD-SOPG-GNPs were found in the MVBs and in LBs (E). (F) After 96 hrs of growth the NBD-SOPG-GNPs were hard to find, but when found they were still in MVBs and LBs.

3.8 Cell number measured by Coulter counter.

Formation of LBs appears to be one response to the exposure of A549 cells to NBD-SOPG-GNPs. The question then arises whether the NBD-SOPG-GNPs inhibit the proliferation of A549 cells.

Table 3.2 shows the total number of live A549 cells measured by particle counter in samples where cells were grown for a total of 72 hrs (about 2 cell cycles) without exposure to NBD-SOPG-GNPs (control) or with exposure to NBD-SOPG-GNPs for the first 24 hrs, for the first 48 hrs, and for the entire 72 hrs. Within experimental error (each experiment was repeated three times, $p>0.1$) the total number of cells is independent of the duration of exposure to the GNPs indicating that cell growth is not inhibited by the exposure to NBD-SOPG-GNPs. We conclude that the nanoparticles are not toxic to the point of inhibiting growth, but equally important; these data also suggest that the cells do not differentiate to a state where they cannot continue to divide.

	Cell number
Control	1.78×10^6
24 h	1.79×10^6
48 h	1.64×10^6
72 h	1.62×10^6

Table 3.2. Numbers of cells per tissue culture dish measured by Coulter counter in cultures grown for 72 hrs with the GNPs initially present for the number of hours indicated in the graph. *Compare cell numbers of control and sample treated with NBD-SOPG-GNPs for 24 hrs, $p>0.1$, ** compare cell numbers of control and sample treated with NBD-SOPG-GNPs for 48 hrs, $p>0.1$, *** compare cell numbers of control and sample treated with NBD-SOPG-GNPs for 72 hrs, $p>0.1$.

Pernodet et al studied the adverse effect of citrate coated gold nanoparticles with the similar size on the human dermal fibroblast cells. [25] They found the proliferation of citrated GNPs is not obvious for the first two days, but becomes proliferation rate decreased dramatically after four days. They found the actin fibers are well spread in the control cells after six days, but the most of the actin fibers density decreased and some of them are disappeared in cells treated with citrate GNPs. [25] As we know, the actin fiber controls the proliferation, differentiation and adhesion of cells. We also observed the actin fiber disruption after the 72 hrs treatment in A549 cells, which may contribute to the cause of the decrease in proliferation.

3.9 The uptake of NBD-SOPG-GNPs in C2C12 cells

3.9.1 NBD-SOPG-GNPs was readily internalized by C2C12 cells

The confocal microscopy images suggest that the NBD-SOPG-GNPs are readily taken up by C2C12 cells and accumulated in peri nuclear area but not the nucleus. Figure 3.10 compares the DIC microscopy images and confocal microscopy images of C2C12 cells prior to and after exposure to NBD-SOPG-GNPs. It is clear from the DIC images that the C2C12 cells treated with NBD-SOPG-GNPs (B-row, C-row) have more vesicular structures than the control cells (A-row). These bright, vesicular structures are not similar in size to the vesicular structures in A549 cells. As showed in Figure 3.10 (C), some of the vesiclular structures are as large as 2-4 μm, but some of them are as small as the vesicles found in A549 cells.

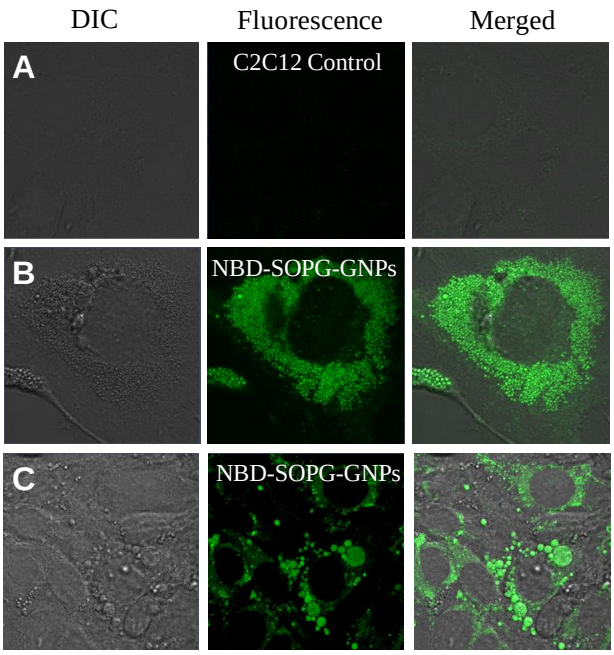

Figure 3.10. The DIC and confocal images of C2C12 control sample (A) and C2C12 cells treated with NBD-SOPG-GNPs for 48 hrs (B, C).

3.9.2 The co-localization studies of NBD-SOPG-GNPs with compartments in C2C12 cells

3.9.2.1 The co-localization studies of NBD-SOPG-GNPs with compartments in C2C12 cells

The three images in Figure 3.11 (A) shows the nucleus in each cell as labeled with DAPI staining (Figure 3.11 Aa, blue color) and it is evident from the merged images (Figure 3.11 Ac) that none of the NBD-SOPG-GNPs (Figure 3.11 Ab, green color) enter the nucleus. The three images in Figure 3.11 (B) shows the lack of co-localization of the green NBD-SOPG-GNPs with mitochondria stained with MitoTracker Red (Figure 3.11 Ba, red colour). The three images in Figure 3.11 (C) compare the intracellular distribution of NBD-SOPG-GNPs and peroxisomes,

which are labeled with the peroxisome kit (Figure 3.11 Ca, red color), and demonstrate clearly that there is no co-localization. [17]

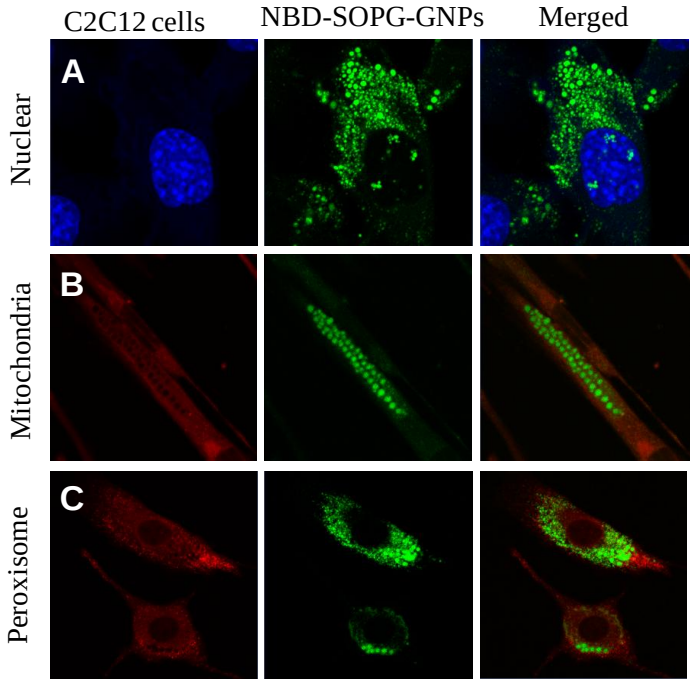

Figure 3.11. Comparison of the localization of NBD-SOPG-GNPs and various intracellular organelles in C2C12 cells. The first column of images shows the intracellular organelles of C2C12 cells, the second column of images shows the distribution of NBD-SOPG-GNPs (green), and the third column are merged images. The GNPs accumulate around the peri-nuclear area, but do not penetrate into the nucleus (A). Likewise, the NBD-SOPG-GNPs are not related to the mitochondria (B) or peroxisomes (C).

3.9.2.2 The co-localization of NBD-SOPG-GNPs with LAMP-1 in C2C12 cells analyzed by image cross correlation spectroscopy

Figure 3.12 illustrates the co-localization of the NBD-SOPG-GNPs with the LAMP-1 protein with time of incubation between 24 hrs and 72 hrs. The extent of

co-localization of the two fluorescent components can be quantified using ICCS. [14, 15] The results of the autocorrelation analyses are shown in Figure 3.13. The co-localization rate of F(r/g) illustrates the fraction of acidic compartments that contain NBD-SOPG-GNPs. And the value of F(g/r) is an estimate of the fraction of the NBD-SOPG-GNPs that are co-located with the acidic compartments. The F(r/g) shows that the fraction of acidic compartments that contain NBD-SOPG-GNPs is close to zero for 24 hrs, 48 hrs and 72 hrs. And F(g/r) also shows no fraction of NBD-SOPG-GNPs is associated with the LAMP-1 protein. This suggests that the NBD-SOPG-GNPs are not related to the LAMP-1 protein in C2C12 cells.

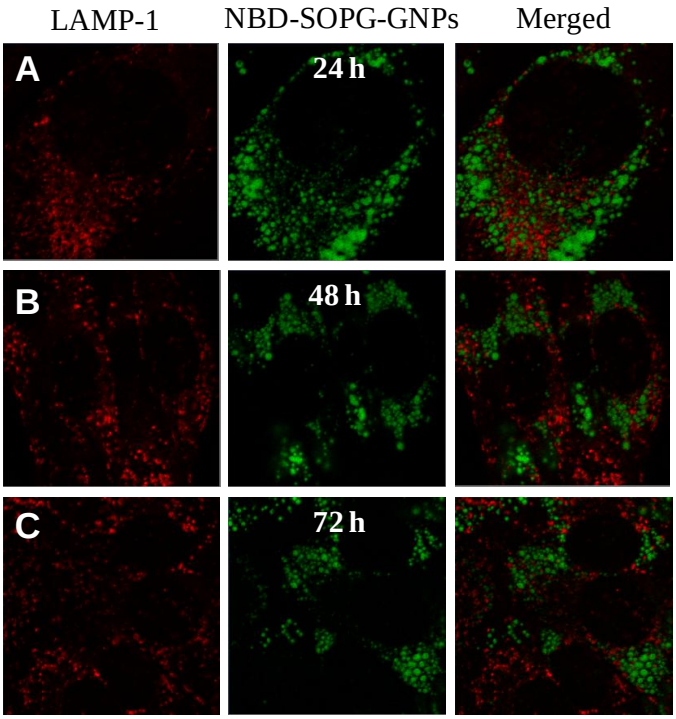

Figure 3.12. The NBD-SOPG-GNPs shows no significant co-localization with LAMP-1 protein after the incubation time of 24 hrs (A), 48 hrs (B) and 72 hrs (C).

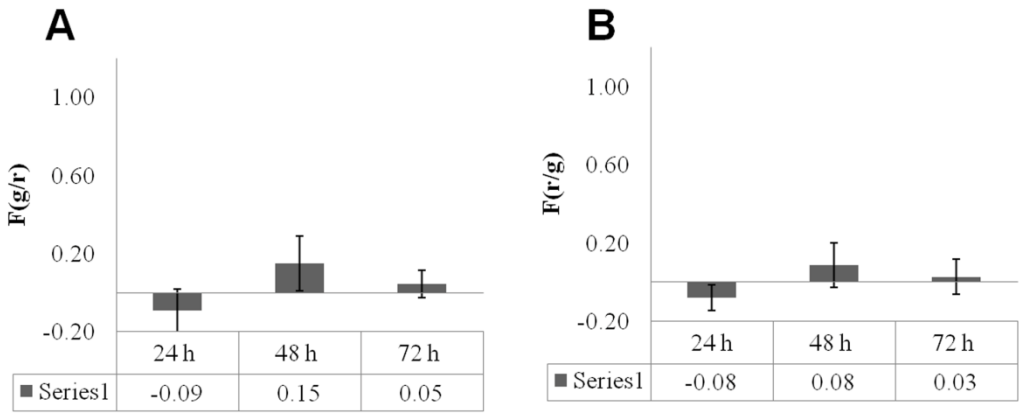

Figure 3.13 (A) The histogram of the co-localization rate F(r/g). (B) The histogram of the co-localization rate F(g/r).

3.9.2.4 The co-localization of NBD-SOPG-GNPs with Lysosome-RFP^{TM} in C2C12 cells

Figure 3.14 (A) illustrates the co-localization of the NBD-SOPG-GNPs with the lysosome which was labeled by Lysosome-RFP^{TM} after the incubation of 24 hrs. It is evident from the merged images that the green NBD-SOPG-GNPs have significant co-localization with lysosome. Figure 3.14 (B) shows that there is no significant co-localization between NBD-SOPG-GNPS and acidic compartments which is labeled by LysoTracker Red after the incubation of 72 hrs.

And in the Figure 3.12, we showed there are almost zero co-localization rates between the NBD-SOPG-GNPs and the LAMP-1 protein. In conclusion, our experiments indicate that the NBD-SOPG-GNPs have great co-localization with lysosome labeled by Lysosome-RFP^{TM}, but have no co-localization with acidic compartments or LAMP-1 protein. In order to have a clear understanding of the localization of NBD-SOPG-GNPs, we need to do more experiments.

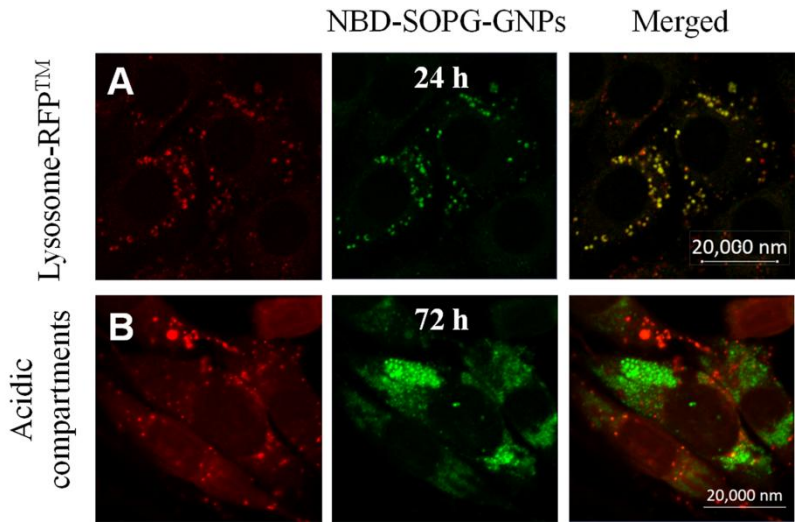

Figure 3.14. The NBD-SOPG-GNPs shows significant co-localization with lysosomes which were labeled by Lysosome-RFP™ after the incubation time of 24 hrs (A) and no co-localization between NBD-SOPG-GNPs and acidic compartments which were labeled by LysoTracker Red after the incubation of 72 hrs (B).

3.9.3 Electron microscope

3.9.3.1 The uptake process of NBD-SOPG-GNPs in C2C12 cells studied by electron microscope

As seen in Figure 3.15 (A), particles are taken up by C2C12 cells and stored in some kind of vesicular structure. It is clear from Figure 3.15 (B) that these vesicular structures are lack of the multimembrane structures which showed in A549 cell. Some of these vesicular structures are around 500 nm, but some of them are as big as 1-2 μm. After 48 hrs, these particles still mainly stay in the vesicular structures.

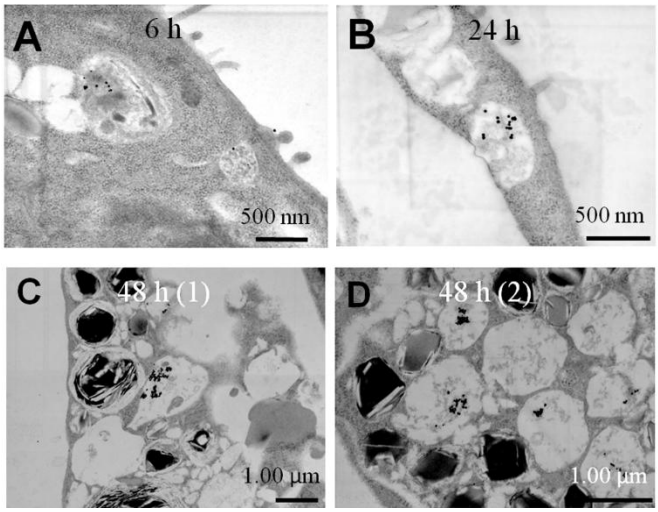

Figure 3.15. Cellular uptake of the 30 nm NBD-SOPG-GNPs into C2C12 cells in different times. Image obtained after 6 hrs (A), 24 hrs (B), and 48 hrs (C, D) of exposure to NBD-SOPG-GNPs.

3.9.3.2 The exocytosis of NBD-SOPG-GNPs in C2C12 cells studied by electron microscope

As seen in Figure 3.16 (A), particles are mainly accumulated in the vesicular structures in C2C12 cells. As the time of growth increase, it is hard to find the particles in cells as shown in Figure 3.16 (C) and (D). There are two possibilities, one is that the population of cells increased fast and the cut cells are mainly new cells without particles. The other possibility is the particles are excreted by cells and cause the number of particles to decrease in cells. However, we need to do more experiments to verify the possibilities.

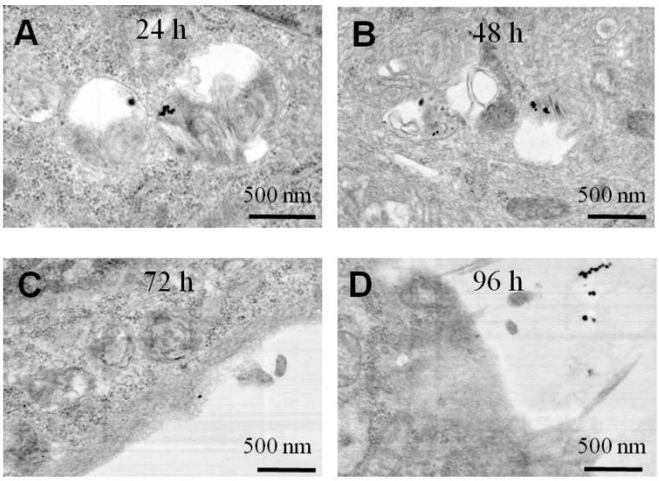

Figure 3.16. Exocytosis of 30 nm NBD-SOPG-GNPs in C2C12 cells depends on time. (A) After 24 hrs of incubation and 24 hrs of growth, a lot of NBD-SOPG-GNPs were found in vesicular structures. (B) After 24 hrs of incubation and 48 hrs of growth, NBD-SOPG-GNPs were still found in the vesicular structure. After 24 hrs incubation and 72 hrs of growth (C) or 96 hrs of growth (D), the NBD-SOPG-GNPs are hard to be found in cells.

3.10 The uptake of NBD-SOPG-GNPs in C2bbe1 cells

3.10.1 NBD-SOPG-GNPs was readily internalized by C2bbe1 cells

The confocal microscopy images suggest that the NBD-SOPG-GNPs are readily taken up by C2bbe1 cells. Figure 3.17 compares the DIC microscopy images and confocal microscopy images of C2bbe1 cells prior to and after exposure to GNPs for 72 hrs. It is clear from Figure 3. 17 (C) that most of the fluorescence vesicular structures are uniform in size and bigger than the vesicular structures in A549 cells. There are some vesicular structures with size around 500 nm as showed in Figure 3.17 (B). However, most of the vesicular structures are around 4-5μm.

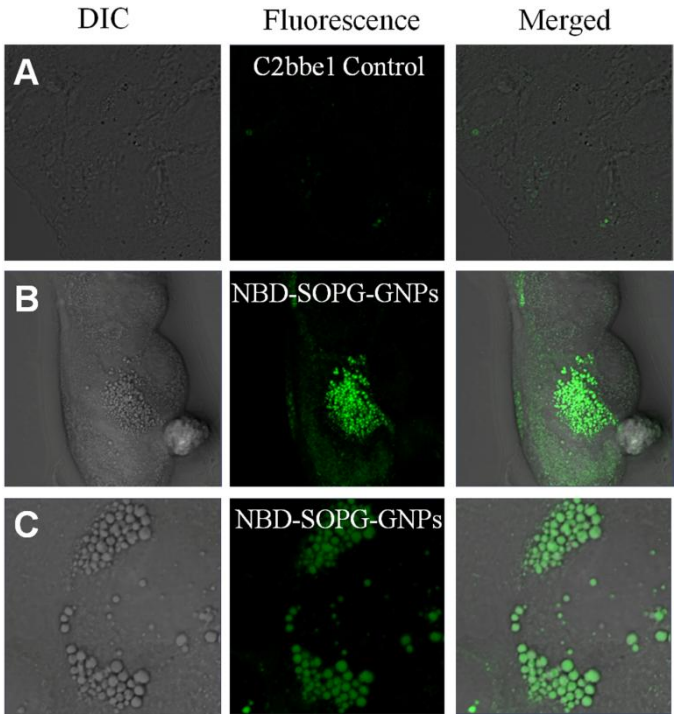

Figure 3.17. The DIC and confocal images of C2bbe1 control sample (A) and C2bbe1 cells treated with NBD-SOPG-GNPs for 72 hrs (B, C).

3.10.2 The co-localization studies of NBD-SOPG-GNPs with compartments in C2bbe1 cells

3.10.2.1 The co-localization studies of NBD-SOPG-GNPs with compartments in C2bbe1 cells

The three images in Figure 3.18 (A) shows the nucleus in each cell as labeled with DAPI staining (Figure 3.18 Aa, blue color) and it is evident from the merged images (Figure 3.18 Ac) that none of the NBD-SOPG-GNPs (Figure 3.18 Ab, green color) enter the nucleus. The three images in Figure 3.18 (B) shows the lack of co-localization of the green NBD-SOPG-GNPs with mitochondria stained with MitoTracker Red (Figure 3.18 Ba, red colour). The three images in Figure 3.18 (C) compare the intracellular distribution of NBD-SOPG-GNPs and peroxisomes,

which are labeled with the peroxisome kit (Figure 3.18 Ca, red color), and demonstrate clearly that there is no co-localization. [17]

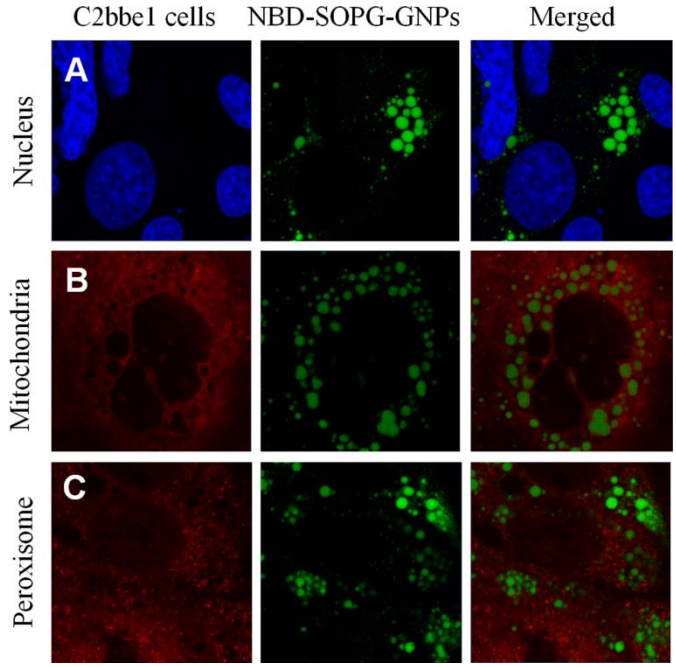

Figure 3.18. Comparison of the localization of NBD-SOPG-GNPs and various intracellular organelles in C2bbe1 cells. The first column of images shows the intracellular organelles of C2bbe1 cells, the second column of images shows the distribution of NBD-SOPG-GNPs (green), and the third column are merged images. The NBD-SOPG-GNPs accumulate around the peri-nuclear area, but do not penetrate into the nucleus (A). Likewise, the NBD-SOPG-GNPs are not related to the mitochondria (B) or peroxisomes (C).

3.10.2.2 The co-localization of NBD-SOPG-GNPs with acidic compartments in C2bbe1 cells

Figure 3.19 illustrates the co-localization of the NBD-SOPG-GNPs with the acidic compartments with the incubation time of 24 hrs. It is evident from the merged images that the green NBD-SOPG-GNPs have no significant co-

localization with acidic compartments. In order to find the location of NBD-SOPG-GNPs in C2bbe1 cells, we need to do more experiments.

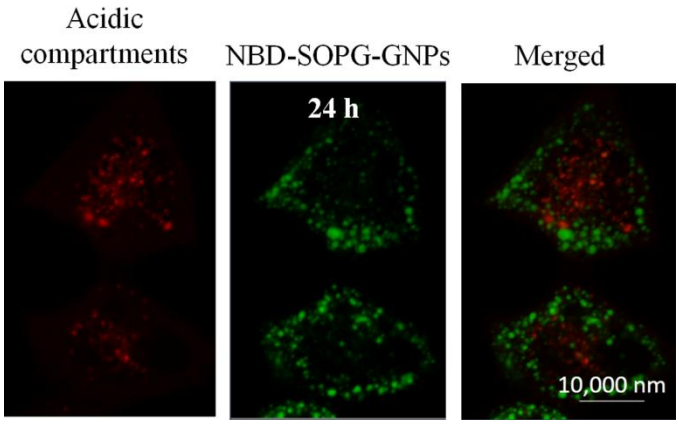

Figure 3.19. The NBD-SOPG-GNPs shows no significant co-localization with acidic compartments after the incubation time of 24 hrs in C2bbe1 cells.

3.10.3 The uptake process of NBD-SOPG-GNPs in C2bbe1 cells studied by electron microscope

As seen in Figure 3.20 (B), particles are taken up by C2bbe1 cells and stored in some small vesicular structure. It is clear from Figure 3.20 (C) that these small vesicular structures become large multivesicular structures with multimembrane. After 24 hrs or 48 hrs, more and more large multivesicular structures are observed. Those vesicular structures could be as large at 5 μm.

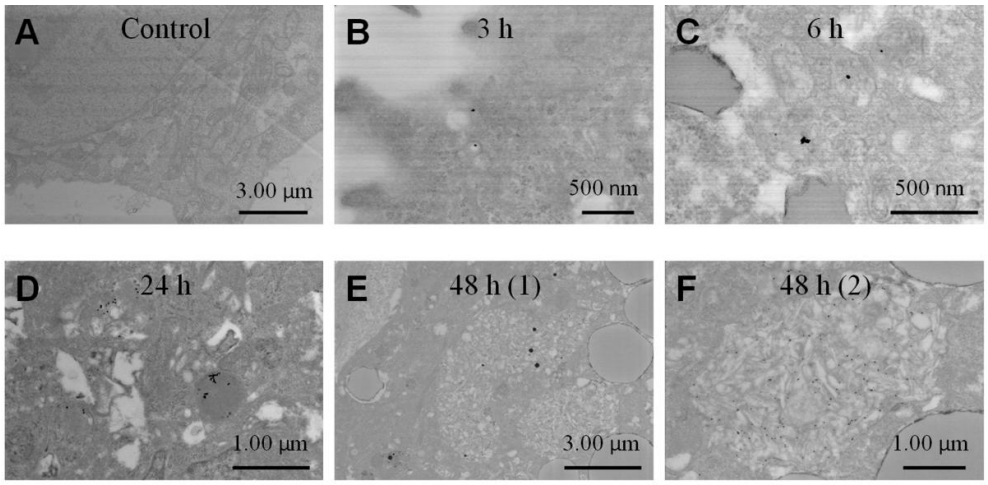

Figure 3.20. Cellular uptake of the 30 n1m NBD-SOPG-GNPs into C2bbe1 cells in different times. (A) Representative image from the control sample. (B) Image obtained after 3 hrs of exposure to NBD-SOPG-GNPs. (C) Image obtained after 6 hrs of exposure to NBD-SOPG-GNPs where they appear in big multivesicular bodies in C2bbe1 cells. (D) Image obtained after 24 hrs of exposure; (E, F) Image obtained after 48 hrs of exposure; large multivesicular bodies are still the main destination to NBD-SOPG-GNPs. Within the vesicles, the NBD-SOPG-GNPs are relatively dispersed.

Reference

1, Daniel, M. C., Astruc, D. Gold Nanoparticles: Assembly, Supramolecular Chemistry, Quantum-Size-Related Properties, and Applications toward Biology, Catalysis, and Nanotechnology. *Chemical Review*. **2004**, 104, 293-346.

2. Huo, Q., Worden, J. G., Monofunctional Gold Nanoparticles: Synthesis and Applications. *Journal of Nanoparticle Research*. **2007**, 9, 1013-1025.

3, Huang, X., Jain, P. K., El-Sayed, I. H. Gold Nanoparticles: Interesting Optical Properties and Recent Applications in Cancer Diagnostics and Therapy. *Nanomedicine (Lond)*. **2007**, 2, 681-93.

4. Nativo, P., Prior, I.A., Brust, M. Uptake and Intracellular Fate of Surface-Modified Gold Nanoparticles. *ACS Nano*. **2008**, 2, 1639-44.

5. Mironava, T., Hadjiargyrou, M., Simon, M. et al. Gold Nanoparticles Cellular Toxicity and Recovery: Effect of Size, Concentration and Exposure time. *Nanotoxicology*. **2010**, 4 120-37.

6. Chithrani, B. D., Chan, W.C. Elucidating the Mechanism of Cellular Uptake and Removal of Protein-Coated Gold Nanoparticles of Different Sizes and Shapes. *Nano letter*. **2007**, 7, 1542-50.

7. Andreeva, A. V., Kutuzov, M. A., Voyno-Yasenetskaya, T. A. Regulation of surfactant secretion in alveolar type II cells. *AJP - Lung Physiol*, **2007**, 293, L259-L271.

8. Lkegami, M., Weaver, T. E., Grant, S. N. et al. Pulmonary Surfactant Surface Tension Influences Alveolar Capillary Shape and Oxygenation. *Am J Respir Cell Mol Biol*., **2009**, 41, 433-439.

9. Schmitz, G., Müller, G. Structure and Function of Lamellar Bodies, Lipid-Protein Complexes Involved in Storage and Secretion of Cellular Lipids. *J Lipid Res*., **1991**, 32, 1539-70.

10. Wissel, H., Lehfeldt, A., Klein, P. et al. Endocytosed SP-A and Surfactant Lipids are Sorted to Different Organelles in Rat type II Pneumocytes. *Am J Physiol Lung Cell Mol Physiol*., **2001**, 281, L345-60.

11. Foster, K. A., Oster, C. G., Mayer, M. M. et al. Characterization of the A549 Cell Line as a Type II Pulmonary Epithelial Cell Model for Drug Metabolism. *Exp Cell Res*., **1998**, 243, 359-66.

12. Afzelius, B. A., Maunsbach, A. B. Biological ultrastructure research; the first 50 years. *Tissue and Cell*., **2004**, 36, 83-94.

13. Griffiths, G. Bringing electron microscopy back into focus for cell biology. *Trends Cell Biol.*, **2001**, 11, 153-154.

14. Srivastava, M., Petersen, N.O. Image cross-correlation spectroscopy: A New Experimental Biophysical Approach to Measurement of Slow Diffusion of Fluorescent Molecules. *Methods in Cell Science*. **1996**, 18, 47-54.

15. Kolin, D.L., Wiseman, P.W. Advances in Image Correlation Spectroscopy: Measuring Number Densities, Aggregation States, and Dynamics of Fluorescently Labeled Macromolecules in Cells. *Cell Biochem Biophys*, **2007**, 49, 141-64.

16. Wang, L., Liu, Y., Li, W. et al. Selective Targeting of Gold Nanorods at the Mitochondria of Cancer Cells: Implications for Cancer Therapy. *Nano Lett*., **2011**, 11, 772-80.

17. Colton, H. M., Falls, J. G., Ni, H. et al. Visualization and Quantitation of Peroxisomes using Fluorescent Nanocrystals: Treatment of Rats and Monkeys with Fibrates and Detection in the Liver. *Toxicol Sci*., **2004**, 80, 183-92.

18. Chander, A., Johnson, R. G., Reicherter, J. et al. Lung Lamellar Bodies Maintain an Acidic Internal pH. *J Biol Chem*., **1986**, 261, 6126-31.

19. Reasor, M. J., Kacew, S. Drug-Induced Phospholipidosis: Are There Functional Consequences? *Exp Biol Med (Maywood)*, **2001**, 226, 825-30.

20. Halliwell, W. H. Cationic Amphiphilic Drug-Induced Phospholipidosis. *Toxicol Pathol*., **1997**, 25, 53-60.

21. Raymond, A. A., Gonzalez de Peredo, A., Stella, A. et al. Lamellar Bodies of Human Epidermis. *Mol Cell Proteomics*. **2008**, 7, 2151-75.

22. Piper, R. C., Luzio, J. P. Late Endosome: Sorting and Partitioning in Multivesicular Bodies. *Traffic*, **2001**, 2, 612-21.

23. Falguières, T., Luyet, P. P., Gruenberg, J. Molecular Assemblies and Membrane Domains in Multivesicular Endosome Dynamics. *Exp Cell Res*., **2009**, 315, 1567-73.

24. Gruenberg, J., Stenmark, H. The Biogenesis of Multivesicular Endosomes. *Nat Rev Mol Cell Biol*., **2004**, 5, 317-23.

25. Pernodet, N., Fang, X., Sun, Y. et al. Adverse effects of citrate/gold nanoparticles on human dermal fibroblasts. *Small*, **2006**, 2, 766-773.

Chapter 4 Future work

4.1 The Fluorescence resonance energy transfer (FRET) between NBD-SOPG-GNPs (green) and DiI-SOPG-GNPs (red)

4.1.1 Basic concepts in fluorescence and FRET

When a molecule is excited to its excited singlet state, it will emit fluorescence to go back to its ground singlet state. The wavelength of photon emission is determined by the energy gap between the excited and ground state. This process is described in the Jablonski diagram in Figure 4.1. [1] The excitation of molecule is usually followed by fast vibrational relaxation and internal conversion, which results in a lower energy of emission and gives rise to a significant red shift. [2]

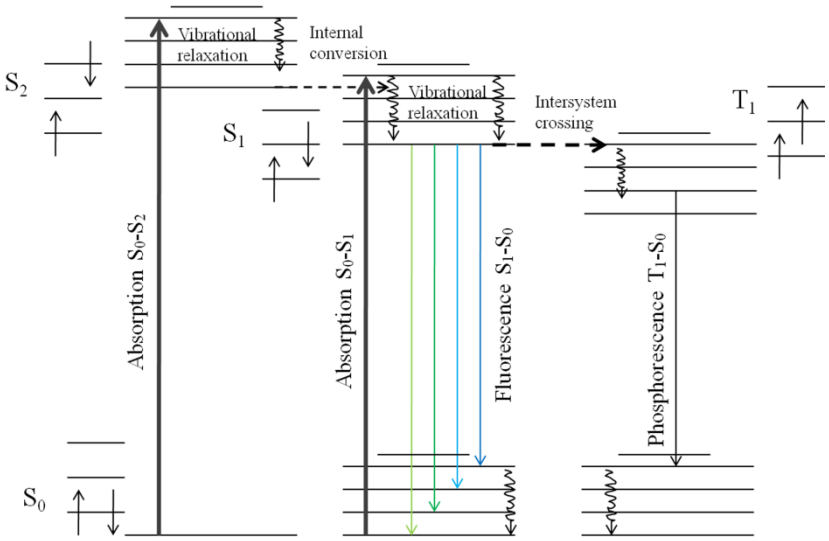

Figure 4.1. Perrin-Jablonski diagram. [3, 4] The S_0, S_1 and S_2 represent the ground, first excited and second excited singlet state. T_1 is the excited triplet state, in which the electrons spin are unpaired (parallel). The vibrational and rotational states of each electronic state are closely packed in energy. [Adapted from reference 1]

The molecule absorbs energy and jumps from S_0 to S_1 or S_0 to S_2, followed by a rapid vibrational relaxation through the interaction with solvents or other molecules. The intersystem crossing conversion can also happen, for example, the relaxation from S_1 to T_1 causes the loss of fluorescence. The phosphorescence transition from T_1 to S_0 takes much longer time than the fluorescence, but faster when it is assisted by the collision of oxygen. [1]

When a second fluorescent molecule is in the proximity, excitation energy of the first molecule can be transferred to the second molecules nonradiatively. (Figure 4.2) This energy transfer is because of the Coulombic coupling of the two transition dipoles and often referred as fluorescence resonance energy transfer (FRET). FRET has a strong dependence of the distance between donor molecule and acceptor molecule, which is usually within 100 Å. [Adapted from reference 5]

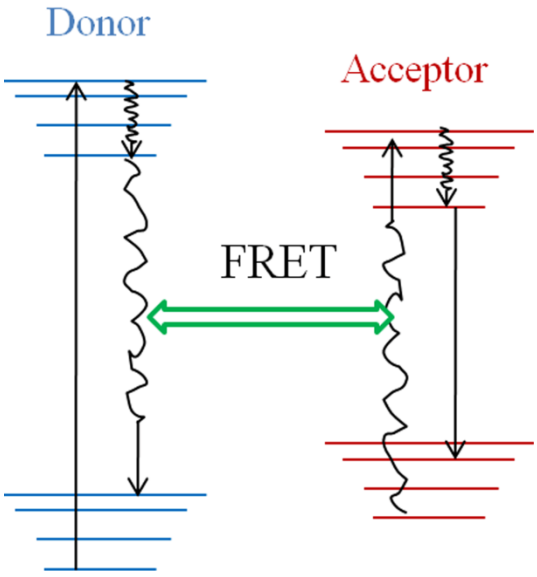

Figure 4.2. Jablonski diagram shows the Förster (fluorescence) resonance energy transfer (FRET) of a donor and acceptor pair. [Adapted from reference 2]

According to Förster theory, the energy transfer rate k_T of FRET is described by:

$$\kappa_T = \kappa_D \times R_0^6 \times r^{-6}$$

where r is the distance between the two chromophores, R_0 is the Förster radius and k_D is the fluorescence decay rate of donor in absence of the acceptor.

The Förster distance R_0 is a parameter depends on the intrinsic and environment properties of the molecules, such as the quantum yield of donor, the integral of the two spectral overlap and the orientation of the two molecules. (Figure 4.3)

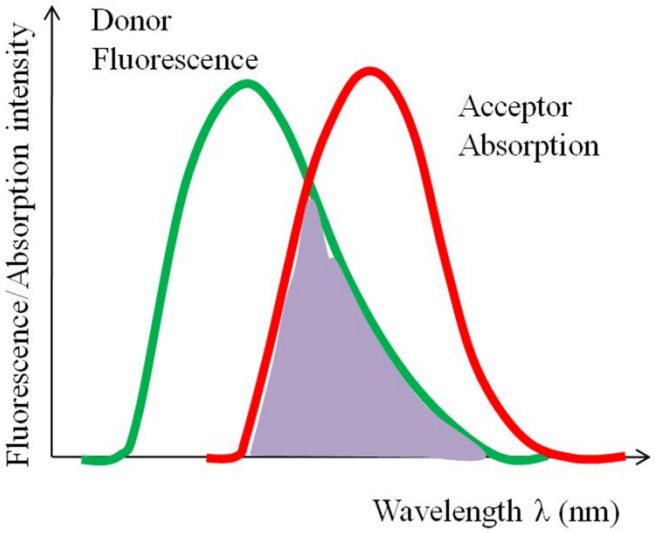

Figure 4.3. The spectral overlap of the donor emission spectrum and the acceptor absorption spectrum. [Adapted from reference 6]

Correspondingly, a transfer efficiency of FRET can be defined as

$$E_{FRET} = \frac{1}{1 + \left(\frac{r}{R_0}\right)^6}$$

The energy transfer efficiency can also be given by:

$$E_{FRET} = 1 - \frac{I_d^{da}}{I_d^d}$$

in which I_d^{da}, I_d^d are the fluorescence intensity of the donor with or without acceptor.

4.1.2 FRET of NBD-SOPG-GNPs (green) and DiI-SOPG-GNPs (red)

The phospholipid bilayer is about 2-4 nm away from the surface of GNPs by the characterization of TEM. If the phospholipid coated GNPs fuse with each other, it may cause aggregation and changes the property of the GNPs. This FRET studies can help us to understand the stability of the phospholipid on the surface of GNPs. In this study, we firstly synthesized the DiI labeled SOPG coated GNPs (DiI-SOPG-GNPs) using the same method as NBD-SOPG-GNPs. [7] In the FRET experiment, NBD-SOPG-GNPs are mixed with DiI-SOPG-GNPs at different concentration and we measure the change of fluorescence intensity at a fixed wavelength. If a significant energy transfer between the two different GNPs is observed, then it means the phospholipid membrane of GNPs fuse with each other in the solutions. We can also add some surfactants to induce the fusion of GNPs, which may serve as a positive control.

Furthermore, we can also study the FRET of NBD-SOPG-GNPs and DiI-SOPG-GNPs in cells because the interior environment of cells is different from the solution. If the phospholipid coated GNPs lost the lipid membrane in cells and result in aggregation, we should see the energy transfer. This will address the question whether the phospholipid coated GNPs lose the membrane or aggregate inside of the cells.

4.2 The quenching of NBD dyes by GNPs

The resonance energy transfer can also occur when an organic dye is close to the surface of the GNPs. [8-10] The absorbance of GNPs depends on the size and shape and is typically around 515 to 530 nm. The maxima emission band of NBD dye locates at approximately 540 nm, which overlaps with the absorbance band of GNPs. Thus, the forming of GNPs in reaction will result in the energy transfer from the dye to GNPs. And this energy transfer efficiency highly depends on 1) the distance between the organic donor molecule and the GNPs; 2) the orientation of the donor dipole relative to the donor-GNPs axis; 3) the spectrum overlap of the donor emission and GNPs absorption. (Figure 4.4) [11]

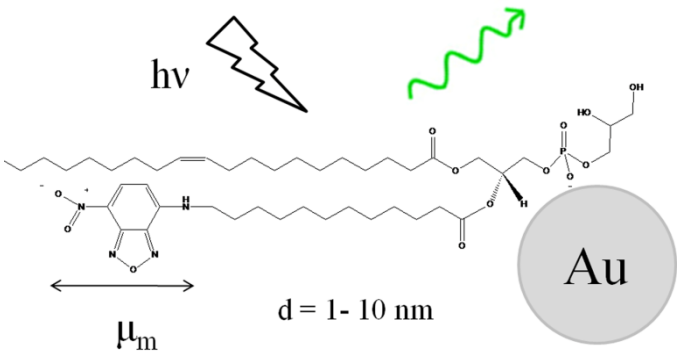

Figure 4.4. NBD-PG dye molecules are attached to the surface of GNPs. The resonant energy transfer depends on the distance of dye molecule to particle surface (d) and the angle of dipole moment μ_m of the dye molecule relative to the dye-nanoparticle axis. [Adapted from reference 11]

As shown in Figure 4.4, the efficiency of the energy transfer depends on the distance between the dye molecule and the GNPs. As shown in the TEM image, the phospholipid bilayer is about 2-4 nm away from the surface of GNPs, which will result in efficient energy transfer.

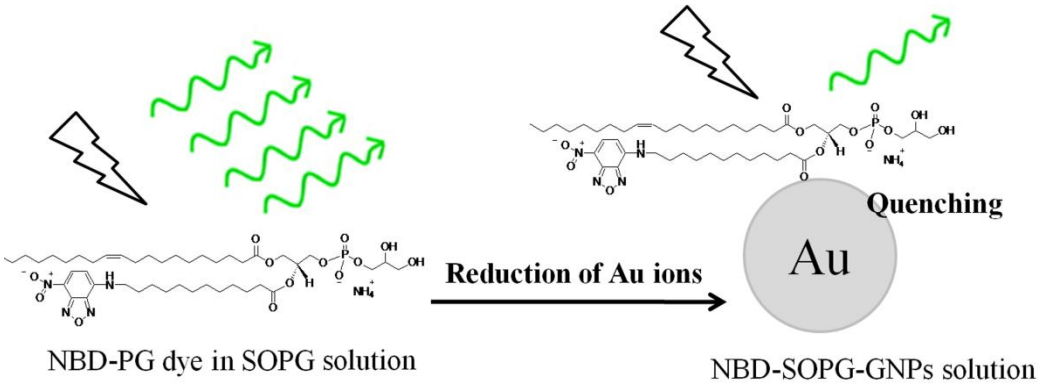

Figure 4.5. Schematic diagram shows the fluorescence quenching of the NBD dye by the formation of GNPs in reaction. The change in the fluorescence intensity of NBD dye can be measured by the fluorescence plate reader. [Adapted from reference 12]

The energy transfer between the NBD dye and the GNPs will give rise to significant quenching of the NBD dye. (Figure 4.5) In order to measure the fluorescence intensity quenching, we can compare the fluorescence intensity of SOPG solution containing NBD-PG molecules before and after the formation of GNPs. The fluoresence intensity can be measured by the fluorescence plate reader at a fixed wavelength. [12]

Another method is to remove the NBD dye from GNPs and measure the recovery of NBD fluorescence intensity. I tried both Triton X-100 and Glutathione (GSH) at different concentration; however, none of them can remove the phospholipid bilayer completely. This experiment also proved the phospholipid bilayer is very stable on the surface of GNPs. In conclusion, we need to find a stronger detergent or proper method to remove the NBD dye from the GNPs totally.

4.3 The uptake pathway inhibited by inhibitors

Endocytosis is an engulfing process of cells to take up extracellular materials. Once internalized, the extracellular materials will encounter different destines by different pathways. For example, extracellular materials may be sent to late endosomes and lysosomes for degradation, or recycled to the plasma membrane in vesicles, or designed to trans Golgi network or ER in cells. [13]

Classically, endocytosis includes two modes: pinocytosis and phagocytosis (Figure 4.6). Pinocytosis is a process in which cells form an invagination to bring small particles or fluid into cells. Phagocytosis is involved in the internalization of big particles, such as bacteria. Pinocytosis can be further split into clathrin mediated endocytosis (CME), caveolae mediated endocytosis (or lipid rafts), and macropinocytosis. CME is the most extensively studied process, in which receptor proteins are involved to select the cargo and initiate the process. This gives rise to the clustering of the ligand-receptor complex in the coated pits formed by clathrin and adaptors. [14] The coated pits pinch off from the plasma membrane and form the clathrin coated vesicles (CCVs). The clathrin coating then depolymerise and releases from the vesicle to produce the early endosome. The early endosome will gradually transform to late endosome by fusing with each other or pre-existing endosomes. The cargoes internalized by this pathway will meet a rapid drop of the pH from 5.9-6.0 (early endosome) to pH 5 during the development from late endosome to lysosomes. [15] The cargoes or ligands will be classified and designated to the suitable cellular compartments, such as lysosomes, Golgi apparatus or plasma membrane.

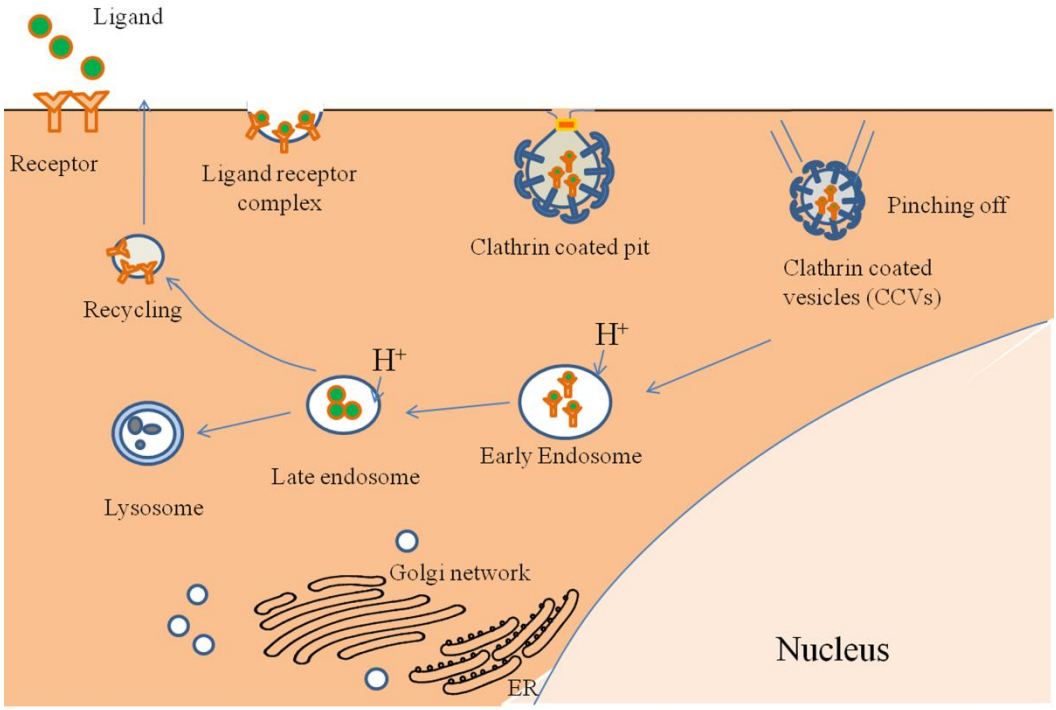

Figure 4.6. Clathrin mediated endocytosis. [Adapted from reference 13]

Caveolae mediated endocytosis is characterized by its connection with the cholesterol-binding proteins called caveolins. [16] Caveolae is defined as a flask shaped invagination which strongly binds to the cholesterol and glycosphingolipids. [17] Caveolae doesn't suffer from the drop of pH, which make it a nonacidic and nondigestive pathway of internalization. [18]

Macropinocytosis is an actin driven and non selective pathway to take up the solute macromolecules. [19] The invaginations of macropinocytosis are relatively large (5 μm) and may vary in size. (Figure 4.7)

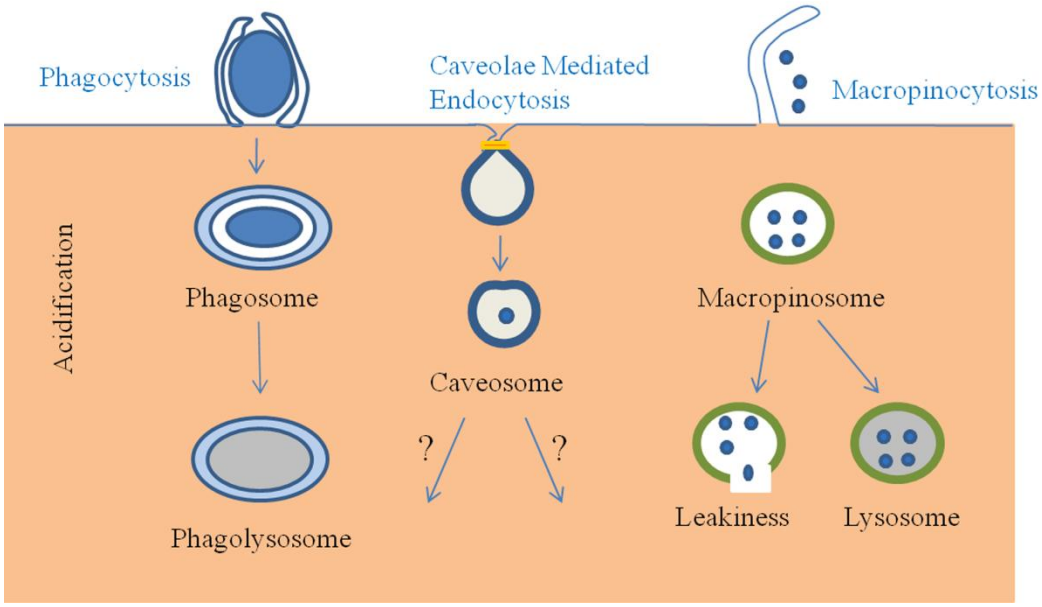

Figure 4.7. Phagocytosis and clathrin independent endocytosis (CIE). [Adapted from reference 13]

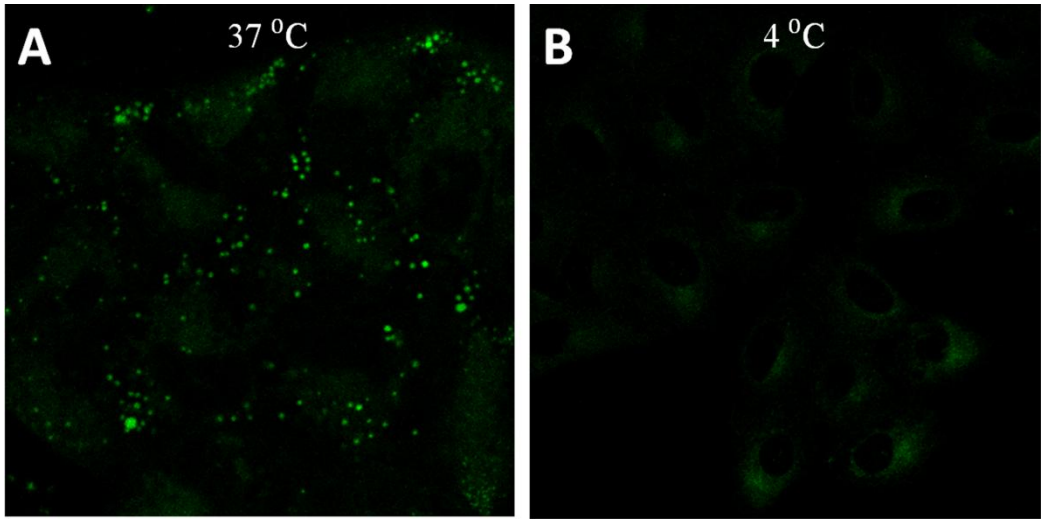

Figure 4.8. The uptake of NBD-SOPG-GNPs is highly inhibited at low temperature in A549 cells. The A549 cells were treated with NBD-SOPG-GNPs at 37 °C (A) and 4 °C (B) for 48 hrs.

A generally useful method to determine the uptake pathway is to treat cells with certain chemical inhibitors. (Table 4.1) However, these inhibitors should be used

with caution because the down regulation of one pathway may cause the up regulation of other pathways. Generally, endocytosis is an energy dependent pathway, and thus can be strongly inhibited by the depletion of ATP or lowing the temperature (4 °C). [20] Figure 4.8 shows that the uptake of NBD-SOPG-GNPs in A549 cells are highly inhibited by the decrease of temperature. CME pathway can be inhibited by the treatments which cause the dissociation of clathrin lattice, for example, chlorpromazine and cytosol acidification. [21] Cytochalasins can bind to the end of the actin filaments and cause the depolymerisation of the actin cytoskeleton, and thus inhibit the actin dependent pathway, such as caveolae mediated endocytosis and macropinocytosis. [22] Nystatin and methyl-cyclodextrin can perturb the caveolae mediated endocytosis by the depletion of the cholesterol. [21] Macropinocytosis can be inhibited by the impairment of the Na^+/H^+ exchange process by amiloride and its analogs. [23] Wortmannin is another inhibitors to macropinocytosis by inhibiting the phosphatidyl inositol-3-phosphate. [24]

Table 4.1. Chemical inhibitors for endocytosis and intracellular trafficking [Adapted from reference 13, 25]

Endocytosis inhibitors	**Pathways targeted**	**Mode of action**
Hypertonic medium	Specific inhibitor of CME	Dissociation of clathrin lattice
Low temperature	General inhibitor of endocytosis	Energy depletion
Metabolic inhibitors	General inhibitor of endocytosis	Energy depletion
Cytosol acidification	Specific inhibitor of CME	Dissociation of clathrin lattice
Potassium depletion	Specific inhibitor of CME	Aggregates clathrin
Chlorpromazine	Specific inhibitor of CME	Translocates clathrin and aP2 from cell surface to endosomes
Chloroquine	Inhibitor of CME	Affects the function of CCVs
Methyl-b-cyclodextrin	Inhibitor of caveolae	Removes cholesterol from plasma membrane
Cytochalasin D	Inhibitor of phagocytosis, macropinocytosis	Depolymerizes F-actin
Amiloride	Inhibitor of macropinocytosis	Inhibit Na+/H+ exchange
Wortmannin	Inhibitor of macropinocytosis	Phosphatidyl inositol-3-phosphate inhibitor
Genestein	Inhibitor of caveolae	Tyrosine kinase inhibitor
Nystatin	Inhibitor of caveolae	Sequester cholesterol
Filipin	Inhibitor of caveolae	Cholesterol binding

CME, clathrin mediated endocytosis; CCVs, clathrin coated vesicles.

This study of uptake pathways is very important because the design of new GNPs based drug delivery system need a thorough understanding of the uptake mechanism. Furthermore, we can promote or inhibit a specific pathway by inhibitors if we know the uptake mechanism. Also, it can help us to understand the cytotoxicity of the lipid coated GNPs. If the lipid coated GNPs could be exported by cells within vesicles, they are less likely to cause serious cytotoxicity. We already compared the uptake of NBD-SOPG-GNPs at 37 °C and 4 °C in A549 cells. In the future, we will apply the inhibitors to inhibit specific pathways. For example, wortmanin, chloroquine and nystatin can be used to inhibit the macropinocytosis, CME and caveolae endocytosis respectively. We can compare the change of fluorescence intensity either by confocal microscopy or flow cytometry. Moreover, it is necessary to measure the cytotoxicity of NBD-SOPG-GNPs and compare it to the citrate coated GNPs or CTAB coated GNPs.

4.4 The co-localization studies of NBD-SOPG-GNPs with lysosome marker in C2C12 cells and C2bbe1 cells

The co-localization study is another useful way to find the uptake mechanism. For example, if the NBD-SOPG-GNPs were found to colocalize with lysosomes, then CME is probably the main pathway. We have found the NBD-SOPG-GNPs have significant co-localization with acidic compartments and lysosomes in A549 cells. However, we need to do more experiments to find the destination of NBD-SOPG-GNPs in C2C12 and C2bbe1 cells.

Reference

1. Clegg, R. M. 1.24 Fluorescence and FRET: Theoretical Concepts 101. Comprehensive *Biophysics*, **2012**, 1, 592-617.
2. Lemke, E. A. 2.05 – Förster Resonance Energy Transfer. *Comprehensive Nanoscience and Technology*, **2011**, 2, 127-151.
3. Lakowicz, J. R. Principles of Fluorescence Spectroscopy (2nd edition.) *Kluwer /Plenum*, New York, **1999**.
4. Valeur, B. Molecular Fluorescence: Principles and Applications. *Wiley-VCH*, Weinheim, **2002**.
5. Latt, S.A., Cheung, H.T., Blout, E.R. Energy transfer - a system with relatively fixed donor–acceptor separation. *Journal of the American Chemical Society*, **1965**, 87, 995-1003.
6. Rolinski, O. J., Mathivanan, C., Mcnaught, G., et al. Structural information on nanomolecular systems revealed by FRET. *Biosensors and Bioelectronics*, **2004**, 20, 424-430.
7. Bakshi, M. S., Possmayer, F., Petersen, N. O. Role of Different Phospholipids in the Synthesis of Pearl-Necklace-Type Gold−Silver Bimetallic Nanoparticles as Bioconjugate Materials. *J. Phys. Chem. C*. **2007**, 111, 14113-14124.
8. Powell, R. D., Halsey, C. M., Spector, D. L., et al. A covalent fluorescent-gold immunoprobe: simultaneous detection of a pre-mRNA splicing factor by light and electron microscopy. *J Histochem Cytochem*. **1997**, 45, 947-56.

9. Tu, Y. Q., Wu, P., Zhang, H., et al. Fluorescence quenching of gold nanoparticles integrating with a conformation-switched hairpin oligonucleotide probe for microRNA detection. *Chem. Commun.* **2012**,48, 10718-10720.
10. Zhang, H., Wang, L., Jiang, W. Label free DNA detection based on gold nanoparticles quenching fluorescence of Rhodamine B. *Talanta*, **2011**, 85, 725-729.
11. Dulkeith, E., Morteani, A. C., Niedereichholz, T., et al. Fluorescence Quenching of Dye Molecules near Gold Nanoparticles: Radiative and Nonradiative Effects. *Phys. Rev. Lett.* **2002**, 89, 203002.
12. Lim, S. Y., Kim, J. H., Lee, J. S., Park, C. B. Gold Nanoparticle Enlargement Coupled with Fluorescence Quenching for Highly Sensitive Detection of Analytes. *Langmuir*, **2009**, 25, 13302-13305.
13. Dutta, D., Donaldson, J. G. Search for inhibitors of endocytosis. *Cellular Logistics*, **2012**, 2, 203-208.
14. Takei, K., Haucke, V. Clathrin-mediated endocytosis: membrane factors pull the trigger. *Trends Cell Biol*. **2001**, 11, 385-391.
15. Maxfield, F. R., McGraw, T. E. Endocytic recycling. *Nat Rev Mol Cell Biol*. **2004**, 5, 121-132.
16. Harris, J., Werling, D., Hope, J. C., et al. Caveolae and caveolin in immune cells: distribution and functions. *Trends Immunol*. **2002**, 23, 158-164.

17. Matveev, S., Li, X., Everson, W., et al. The role of caveolae and caveolin in vesicle-dependent and vesicle-independent trafficking. *Adv Drug Deliv Rev*. **2001**, 49, 237-250.
18. Ferrari, A., Pellegrini, V., Arcangeli, C., et al. Caveolae-mediated internalization of extracellular HIV-1 tat fusion proteins visualized in real time. *Mol Ther*. **2003**, 8, 284-294.
19. Conner, S. D., Schmid, S. L. Regulated portals of entry into the cell. *Nature (Lond)*. **2003**, 422, 37-44.
20. Saraste, J., Palade, G. E., Farquhar, M. G. Temperature-sensitive steps in the transport of secretory proteins through the Golgi complex in exocrine pancreatic cells. *Proc Natl Acad Sci USA*, **1986**, 83, 6425-6429.
21. Lamaze, C., Schmid, S. L. The emergence of clathrin-independent pinocytic pathways. *Curr Opin Cell Biol*. **1995**, 7, 573-580.
22. Parton, R. G., Joggerst, B., Simons, K. Regulated internalization of caveolae. *J Cell Biol*. **1994**, 127, 1199-1215.
23. Hewlett, L. J., Prescott, A. R., Watts, C. The coated pit and macropinocytic pathways serve distinct endosome populations. *J Cell Biol*. **1994**, 124, 689-703.
24. Arcaro, A., Wymann, M. P. Wortmannin is a potent phosphatidylinositol 3-kinase inhibitor: the role of phosphatidylinositol 3,4,5-trisphosphate in neutrophil responses. *Biochem J*. **1993**, 296, 297-301.
25. Khalil, I. A., Kogure, K., Akita, H., et al. Uptake Pathways and Subsequent Intracellular Trafficking in Nonviral Gene Delivery. The

American Society for Pharmacology and Experimental Therapeutics. *Pharmacol Rev*. **2006**, 58, 32-45.